

Simulation of the background from $^{13}\text{C}(\alpha, n)^{16}\text{O}$ reaction in the JUNO scintillator

JUNO Collaboration^a

Thomas Adam³⁷, Kai Adamowicz⁴⁰, Shakeel Ahmad⁵⁷, Rizwan Ahmed⁵⁷, Sebastiano Aiello⁴⁷, Fengpeng An¹⁶, Costas Andreopoulos⁶⁵, Giuseppe Andronico⁴⁷, Nikolay Anfimov⁵⁸, Vito Antonelli⁴⁹, Tatiana Antoshkina⁵⁸, João Pedro Athayde Marcondes de André³⁷, Didier Auguste³⁵, Weidong Bai¹⁶, Nikita Balashov⁵⁸, Andrea Barresi⁵⁰, Davide Basilico⁴⁹, Eric Baussan³⁷, Marco Beretta⁴⁹, Antonio Bergnoli⁵², Nikita Bessonov⁵⁸, Daniel Bick⁴¹, Lukas Bieger⁴⁶, Svetlana Biktemerova⁵⁸, Thilo Birkenfeld⁴⁰, Simon Blyth⁸, Anastasia Bolshakova⁵⁸, Mathieu Bongrand³⁹, Matteo Borghesi⁵⁰, Dominique Breton³⁵, Augusto Brigatti⁴⁹, Riccardo Brugnera⁵³, Riccardo Bruno⁴⁷, Marcel Büchner⁴³, Antonio Budano⁵⁶, Jose Busto³⁸, Anatael Cabrera³⁵, Barbara Caccianiga⁴⁹, Hao Cai²⁶, Xiao Cai⁸, Yanke Cai⁸, Zhiyan Cai⁸, Stéphane Callier³⁶, Steven Calvez³⁹, Antonio Cammi⁵¹, Chuanya Cao⁸, Guofu Cao⁸, Jun Cao⁸, Yaoqi Cao⁶⁶, Rossella Caruso⁴⁷, Cédric Cerna³⁶, Vanessa Cerrone^{53,52}, Jinfan Chang⁸, Yun Chang³¹, Auttakit Chatrabhuti⁶², Chao Chen⁸, Guoming Chen²², Jiahui Chen⁸, Jian Chen¹⁶, Jing Chen¹⁶, Junyou Chen²², Pingping Chen¹⁴, Shaomin Chen¹⁰, Shiqiang Chen²¹, Xin Chen^{21,8}, Yiming Chen⁸, Yixue Chen⁹, Yu Chen¹⁶, Ze Chen^{45,43}, Zhangming Chen²³, Zhiyuan Chen⁸, Jie Cheng⁹, Yaping Cheng⁷, Yu Chin Cheng³², Alexander Chepurnov^{60,59}, Alexey Chetverikov⁵⁸, Davide Chiesa⁵⁰, Pietro Chimenti³, Po-Lin Chou³⁰, Ziliang Chu⁸, Artem Chukanov⁵⁸, Gérard Claverie³⁶, Catia Clementi⁵⁴, Barbara Clerbaux², Claudio Coletta⁵⁰, Selma Conforti Di Lorenzo³⁶, Simon Csakli⁴⁴, Chenyang Cui⁸, Olivia Dalager⁶⁷, Christophe De La Taille³⁶, Zhi Deng¹⁰, Ziyang Deng⁸, Xiaoyu Ding²⁰, Xuefeng Ding⁸, Yayun Ding⁸, Bayu Dirgantara⁶⁴, Carsten Dittrich⁴⁴, Sergey Dmitrievsky⁵⁸, David Doerflinger⁴⁴, Dmitry Dolzhikov⁵⁸, Haojie Dong⁸, Jianmeng Dong¹⁰, Evgeny Doroshkevich⁵⁹, Marcos Dracos³⁷, Frédéric Druillolle³⁶, Ran Du⁸, Shuxian Du²⁹, Yujie Duan²⁶, Katherine Dugas⁶⁷, Stefano Dusini⁵², Hongyue Duyang²⁰, Jessica Eck⁴⁶, Timo Enqvist³⁴, Andrea Fabbri⁵⁶, Ulrike Fahrenholz⁴⁴, Lei Fan⁸, Jian Fang⁸, Wenxing Fang⁸, Dmitry Fedoseev⁵⁸, Li-Cheng Feng³⁰, Qichun Feng¹⁷, Federico Ferraro⁴⁹, Daniela Fetzter⁴³, Marcellin Fotzé³⁷, Amélie Fournier³⁶, Aaron Freegard²³, Feng Gao², Alberto Garfagnini⁵³, Arsenii Gavrikov^{53,52}, Marco Giammarchi⁴⁹, Nunzio Giudice⁴⁷, Maxim Gonchar⁵⁸, Guanghua Gong¹⁰, Hui Gong¹⁰, Yuri Gornushkin⁵⁸, Marco Grassi⁵³, Maxim Gromov^{60,58}, Vasily Gromov⁵⁸, Minghao Gu⁸, Xiaofei Gu²⁹, Yu Gu¹⁵, Mengyun Guan⁸, Yuduo Guan⁸, Nunzio Guardone⁴⁷, Rosa Maria Guizzetti⁵³, Cong Guo⁸, Wanlei Guo⁸, Caren Hagner⁴¹, Hechong Han⁸, Ran Han⁷, Yang Han¹⁶, Jinhong He²⁶, Miao He⁸, Wei He⁸, Xinhai He⁸, Ziou He⁶⁶, Tobias Heinz⁴⁶, Patrick Hellmuth³⁶, Yuekun Heng⁸, YuenKeung Hor¹⁶, Shaojing Hou⁸, Yee Hsiung³², Bei-Zhen Hu³², Hang Hu¹⁶, Jun Hu⁸, Tao Hu⁸, Yuxiang Hu⁸, Guihong Huang¹⁹, Jinhao Huang⁸, Junting Huang²³, Kaixuan Huang¹⁶, Shengheng Huang¹⁹, Tao

Huang¹⁶, Xin Huang⁸, Xingtao Huang²⁰, Yongbo Huang²², Jiaqi Hui²³, Lei Huo¹⁷, Cédric Huss³⁶, Safer Hussain⁵⁷, Leonard Imbert³⁹, Ara Ioannisian¹, Adrienne Jacobi⁶⁷, Arshak Jafar⁴³, Beatrice Jelmini⁵³, Xiangpan Ji²⁵, Xiaolu Ji⁸, Huihui Jia²⁵, Junji Jia²⁶, Cailian Jiang²¹, Wei Jiang⁸, Xiaoshan Jiang⁸, Xiaozhao Jiang⁸, Yijian Jiang⁹, Yixuan Jiang⁸, Xiaoping Jing⁸, Cécile Jollet³⁶, Li Kang¹⁴, Rebin Karaparabil³⁷, Narine Kazarian¹, Ali Khan⁵⁷, Amina Khatun^{2,61}, Khanchai Khosonthongkee⁶⁴, Denis Korablev⁵⁸, Konstantin Kouzakov⁶⁰, Alexey Krasnoperov⁵⁸, Sergey Kuleshov⁵, Sindhujha Kumaran⁶⁷, Nikolay Kutovskiy⁵⁸, Loïc Labit³⁶, Tobias Lachenmaier⁴⁶, Haojing Lai²³, Cecilia Landini⁴⁹, Sébastien Leblanc³⁶, Matthieu Lecocq³⁶, Frederic Lefevre³⁹, Ruiting Lei¹⁴, Rupert Leitner³³, Jason Leung³⁰, Demin Li²⁹, Fei Li⁸, Fule Li¹⁰, Gaosong Li⁸, Hongjian Li⁸, Huang Li⁸, Jiajun Li¹⁶, Min Li³⁷, Nan Li¹², Qingjiang Li¹², Ruhui Li⁸, Rui Li²³, Shanfeng Li¹⁴, Tao Li¹⁶, Teng Li²⁰, Weidong Li^{8,11}, Xiaonan Li⁸, Yi Li¹⁴, Yichen Li⁸, Yifan Li⁸, Yufeng Li⁸, Zhaohan Li⁸, Zhibing Li¹⁶, Zi-Ming Li²⁹, Zonghai Li²⁶, An-An Liang³⁰, Jiajun Liao¹⁶, Minghua Liao¹⁶, Yilin Liao²³, Ayut Limphirat⁶⁴, Bo-Chun Lin³⁰, Guey-Lin Lin³⁰, Shengxin Lin¹⁴, Tao Lin⁸, Xianhao Lin²¹, Xingyi Lin²², Jiajie Ling¹⁶, Xin Ling¹⁸, Ivano Lippi⁵², Caimei Liu⁸, Fang Liu⁹, Fengcheng Liu⁹, Haidong Liu²⁹, Haotian Liu²⁶, Hongbang Liu²², Hongjuan Liu¹⁸, Hongtao Liu¹⁶, Hongyang Liu⁸, Jianglai Liu^{23,24}, Jiayi Liu⁸, Jinchang Liu⁸, Kainan Liu¹⁹, Min Liu¹⁸, Qian Liu¹¹, Runxuan Liu^{45,40}, Shenghui Liu⁸, Shulin Liu⁸, Xiaowei Liu¹⁶, Xiwen Liu²², Xuewei Liu¹⁰, Yankai Liu²⁷, Zhen Liu⁸, Lorenzo Loi⁵⁰, Alexey Lokhov^{60,59}, Paolo Lombardi⁴⁹, Claudio Lombardo⁴⁷, Kai Loo³⁴, Haoqi Lu⁸, Junguang Lu⁸, Meishu Lu⁴⁴, Peizhi Lu¹⁶, Shuxiang Lu²⁹, Xianguo Lu⁶⁶, Bayarto Lubsandorzhev⁵⁹, Sultim Lubsandorzhev⁵⁹, Livia Ludhova^{45,43}, Arslan Lukanov⁵⁹, Fengjiao Luo¹⁸, Guang Luo¹⁶, Jianyi Luo¹⁶, Shu Luo²⁸, Wuming Luo⁸, Xiaojie Luo⁸, Vladimir Lyashuk⁵⁹, Bangzheng Ma²⁰, Bing Ma²⁹, Qiumei Ma⁸, Si Ma⁸, Wing Yan Ma²⁰, Xiaoyan Ma⁸, Xubo Ma⁹, Jihane Maalmi³⁵, Jingyu Mai¹⁶, Marco Malabarba^{45,43}, Yury Malyshkin^{45,43}, Roberto Carlos Mandujano⁶⁷, Fabio Mantovani⁴⁸, Xin Mao⁷, Stefano M. Mari⁵⁶, Agnese Martini⁵⁵, Matthias Mayer⁴⁴, Davit Mayilyan¹, Yue Meng²³, Anselmo Meregaglia³⁶, Lino Miramonti⁴⁹, Marta Colomer Molla², Michele Montuschi⁴⁸, Cristobal Morales Reveco^{45,40,43}, Iwan Morton-Blake²⁴, Massimiliano Nastasi⁵⁰, Dmitry V. Naumov⁵⁸, Elena Naumova⁵⁸, Igor Nemchenok⁵⁸, Elisabeth Neuerburg⁴⁰, Minh Thuan Nguyen Thi³⁰, Alexey Nikolaev⁶⁰, Feipeng Ning⁸, Zhe Ning⁸, Yujie Niu⁸, Hiroshi Nunokawa⁴, Juan Pedro Ochoa-Ricoux^{67,5}, Sebastian Olivares⁶, Alexander Olshevskiy⁵⁸, Domizia Orestano⁵⁶, Fausto Ortica⁵⁴, Rainer Othegraven⁴³, Yifei Pan¹⁶, Alessandro Paoloni⁵⁵, George Parker⁴³, Yatian Pei⁸, Luca Pelicci⁴⁹, Anguo Peng¹⁸, Yu Peng⁸, Zhaoyuan Peng⁸, Elisa Percalli⁴⁹, Willy Perrin³⁷, Frédéric Perrot³⁶, Pierre-Alexandre Petitjean², Fabrizio Petrucci⁵⁶, Oliver Pilarczyk⁴³, Artyom Popov⁶⁰, Pascal Poussot³⁷, Ezio Previtali⁵⁰, Fazhi Qi⁸, Ming Qi²¹, Xiaohui Qi⁸, Sen Qian⁸, Xiaohui Qian⁸, Zhonghua Qin⁸, Shoukang Qiu¹⁸, Manhao Qu²⁹, Zhenning Qu⁸, Gioacchino Ranucci⁴⁹, Thomas Raymond³⁷, Alessandra Re⁴⁹, Abdel Rebi³⁶, Mariia Redchuk⁵², Bin Ren¹⁴, Yuhan Ren⁸, Barbara Ricci⁴⁸, Komkrit Rientong⁶², Mariam Rifai^{45,40,43}, Mathieu Roche³⁶, Narongkiat Rodphai⁸, Fernanda de Faria Rodrigues⁸, Aldo Romani⁵⁴, Bedřich Roskovec³³, Arseniy Rybnikov⁵⁸, Andrey Sadovsky⁵⁸, Paolo Saggese⁴⁹, Deshan Sandanayake³⁷, Anut Sangka⁶³,

Giuseppe Sava⁴⁷, Utane Sawangwit⁶³, Michaela Schever⁴⁰, Cédric Schwab³⁷, Konstantin Schweizer⁴⁴, Alexandr Selyunin⁵⁸, Andrea Serafini⁵³, Mariangela Settimo³⁹, Junyu Shao⁸, Vladislav Sharov⁵⁸, Hangyu Shi¹⁶, Hexi Shi^{45,42}, Jingyan Shi⁸, Yanan Shi⁸, Vitaly Shutov⁵⁸, Andrey Sidorenkov⁵⁹, Fedor Šimkovic⁶¹, Apeksha Singhal^{45,43}, Chiara Sirignano⁵³, Jaruchit Siripak⁶⁴, Monica Sisti⁵⁰, Oleg Smirnov⁵⁸, Sergey Sokolov⁵⁸, Julanan Songwadhana⁶⁴, Boonrucksar Soonthornthum⁶³, Albert Sotnikov⁵⁸, Warintorn Sreethawong⁶⁴, Achim Stahl⁴⁰, Luca Stanco⁵², Elia Stanescu Farilla⁵⁶, Konstantin Stankevich⁶⁰, Hans Steiger^{44,43}, Jochen Steinmann⁴⁰, Tobias Sterr⁴⁶, Virginia Strati⁴⁸, Mikhail Strizh^{60,59}, Alexander Studenikin⁶⁰, Aoqi Su²⁹, Jun Su¹⁶, Guangbao Sun²⁶, Mingxia Sun⁸, Shifeng Sun⁹, Xilei Sun⁸, Yongzhao Sun⁸, Zhengyang Sun²⁴, Narumon Suwonjandee⁶², Akira Takenaka²⁴, Xiaohan Tan²⁰, Jian Tang¹⁶, Jingzhe Tang²², Qiang Tang¹⁶, Quan Tang¹⁸, Xiao Tang⁸, Vidhya Thara Hariharan⁴¹, Yuxin Tian²⁴, Igor Tkachev⁵⁹, Tomas Tmej³³, Marco Danilo Claudio Torri⁴⁹, Andrea Triossi⁵³, Wladyslaw Trzaska³⁴, Yu-Chen Tung³², Cristina Tuve⁴⁷, Nikita Ushakov⁵⁹, Carlo Venettacci⁵⁶, Giuseppe Verde⁴⁷, Maxim Vialkov⁶⁰, Benoit Viaud³⁹, Cornelius Moritz Vollbrecht^{45,40}, Vit Vorobel³³, Dmitriy Voronin⁵⁹, Lucia Votano⁵⁵, Caishen Wang¹⁴, Chung-Hsiang Wang³¹, En Wang²⁹, Hanwen Wang⁸, Jiabin Wang²⁰, Jun Wang¹⁶, Li Wang^{29,8}, Meng Wang¹⁸, Meng Wang²⁰, Mingyuan Wang⁸, Qianchuan Wang²⁶, Ruiguang Wang⁸, Sibao Wang⁸, Tianhong Wang¹⁷, Wei Wang¹⁶, Wenshuai Wang⁸, Xi Wang¹², Yangfu Wang⁸, Yaoguang Wang²⁰, Yi Wang⁸, Yi Wang¹⁰, Yifang Wang⁸, Yuanqing Wang¹⁰, Yuyi Wang¹⁰, Zhe Wang¹⁰, Zheng Wang⁸, Zhimin Wang⁸, Apimook Watcharangkool⁶³, Wei Wei⁸, Wei Wei²⁰, Yadong Wei¹⁴, Yuehuan Wei¹⁶, Zhengbao Wei²², Liangjian Wen⁸, Jun Weng¹⁰, Christopher Wiebusch⁴⁰, Rosmarie Wirth⁴¹, Bi Wu¹⁶, Chengxin Wu¹⁶, Diru Wu⁸, Qun Wu²⁰, Yinhui Wu⁸, Yiyang Wu¹⁰, Zhaoxiang Wu⁸, Zhi Wu⁸, Michael Wurm⁴³, Jacques Wurtz³⁷, Dongmei Xia¹³, Shishen Xian²⁴, Ziqian Xiang²³, Fei Xiao⁸, Pengfei Xiao⁸, Xiang Xiao¹⁶, Wei-Jun Xie³⁰, Xiaochuan Xie²², Yijun Xie⁸, Yuguang Xie⁸, Zhao Xin⁸, Zhizhong Xing⁸, Benda Xu¹⁰, Cheng Xu¹⁸, Donglian Xu^{24,23}, Fanrong Xu¹⁵, Jiayang Xu⁸, Jilei Xu⁸, Jinghuan Xu²², Meihang Xu⁸, Shiwen Xu⁸, Xunjie Xu⁸, Yin Xu²⁵, Yu Xu¹⁶, Jingqin Xue⁸, Baojun Yan⁸, Qiyu Yan^{11,66}, Taylor Yan⁶⁴, Xiongbo Yan⁸, Yupeng Yan⁶⁴, Changgen Yang⁸, Chengfeng Yang¹⁶, Fengfan Yang⁸, Jie Yang²⁹, Lei Yang¹⁴, Pengfei Yang¹⁶, Xiaoyu Yang⁸, Yifan Yang², Yixiang Yang⁸, Zekun Yang²⁰, Haifeng Yao⁸, Jiakuan Ye⁸, Mei Ye⁸, Ziping Ye²⁴, Frédéric Yermia³⁹, Jilong Yin⁸, Weiqing Yin⁸, Xiaohao Yin¹⁶, Zhengyun You¹⁶, Boxiang Yu⁸, Chiye Yu¹⁴, Chunxu Yu²⁵, Hongzhao Yu⁸, Peidong Yu⁸, Xianghui Yu²⁵, Zeyuan Yu⁸, Zezhong Yu⁸, Cenxi Yuan¹⁶, Chengzhuo Yuan⁸, Zhaoyang Yuan⁸, Zhenxiong Yuan¹⁰, Noman Zafar⁵⁷, Kirill Zamogilnyi⁶⁰, Jilberto Zamora⁶, Vitalii Zavadskyi⁵⁸, Fanrui Zeng²⁰, Shan Zeng⁸, Tingxuan Zeng⁸, Liang Zhan⁸, Yonghua Zhan¹⁶, Aiqiang Zhang¹⁰, Bin Zhang²⁹, Binting Zhang⁸, Feiyang Zhang²³, Han Zhang⁸, Hangchang Zhang⁸, Haosen Zhang⁸, Honghao Zhang¹⁶, Jialiang Zhang²¹, Jiawen Zhang⁸, Jie Zhang⁸, Jingbo Zhang¹⁷, Junwei Zhang²², Lei Zhang²¹, Ping Zhang²³, Qingmin Zhang²⁷, Rongping Zhang⁸, Shiqi Zhang¹⁶, Shuihan Zhang⁸, Siyuan Zhang²², Tao Zhang²³, Xiaomei Zhang⁸, Xin Zhang⁸, Xu Zhang⁸, Xuantong Zhang⁸, Yibing Zhang⁸, Yinhong Zhang⁸, Yiyu Zhang⁸, Yongpeng Zhang⁸, Yu Zhang⁸,

**Yuanyuan Zhang²⁴, Yumei Zhang¹⁶, Zhenyu Zhang²⁶, Zhijian Zhang¹⁴,
Jie Zhao⁸, Runze Zhao⁸, Shujun Zhao²⁹, Tianhao Zhao⁸, Hua Zheng¹⁴,
Yangheng Zheng¹¹, Li Zhou⁸, Shun Zhou⁸, Tong Zhou⁸, Xiang Zhou²⁶,
Xing Zhou⁸, Jingsen Zhu¹⁶, Kangfu Zhu²⁷, Kejun Zhu⁸, Zhihang Zhu⁸,
Bo Zhuang⁸, Honglin Zhuang⁸, Liang Zong¹⁰, Jiaheng Zou⁸**

¹ Yerevan Physics Institute, Yerevan, Armenia

² Université Libre de Bruxelles, Brussels, Belgium

³ Universidade Estadual de Londrina, Londrina, Brazil

⁴ Pontificia Universidade Católica do Rio de Janeiro, Rio de Janeiro, Brazil

⁵ Millennium Institute for SubAtomic Physics at the High-energy Frontier (SAPHIR), ANID, Chile

⁶ Universidad Andres Bello, Fernandez Concha 700, Chile

⁷ Beijing Institute of Spacecraft Environment Engineering, Beijing, China

⁸ Institute of High Energy Physics, Beijing, China

⁹ North China Electric Power University, Beijing, China

¹⁰ Tsinghua University, Beijing, China

¹¹ University of Chinese Academy of Sciences, Beijing, China

¹² College of Electronic Science and Engineering, National University of Defense Technology, Changsha, China

¹³ Chongqing University, Chongqing, China

¹⁴ Dongguan University of Technology, Dongguan, China

¹⁵ Jinan University, Guangzhou, China

¹⁶ Sun Yat-Sen University, Guangzhou, China

¹⁷ Harbin Institute of Technology, Harbin, China

¹⁸ The Radiochemistry and Nuclear Chemistry Group in University of South China, Hengyang, China

¹⁹ Wuyi University, Jiangmen, China

²⁰ Shandong University, Jinan, China, and Key Laboratory of Particle Physics and Particle Irradiation of Ministry of Education, Shandong University, Qingdao, China

²¹ Nanjing University, Nanjing, China

²² Guangxi University, Nanning, China

²³ School of Physics and Astronomy, Shanghai Jiao Tong University, Shanghai, China

²⁴ Tsung-Dao Lee Institute, Shanghai Jiao Tong University, Shanghai, China

²⁵ Nankai University, Tianjin, China

²⁶ Wuhan University, Wuhan, China

²⁷ Xi'an Jiaotong University, Xi'an, China

²⁸ Xiamen University, Xiamen, China

²⁹ School of Physics and Microelectronics, Zhengzhou University, Zhengzhou, China

³⁰ Institute of Physics, National Yang Ming Chiao Tung University, Hsinchu

³¹ National United University, Miao-Li

³² Department of Physics, National Taiwan University, Taipei

³³ Charles University, Faculty of Mathematics and Physics, Prague, Czech Republic

³⁴ University of Jyväskylä, Department of Physics, Jyväskylä, Finland

³⁵ IJCLab, Université Paris-Saclay, CNRS/IN2P3, 91405 Orsay, France

³⁶ Univ. Bordeaux, CNRS, LP2I, UMR 5797, F-33170 Gradignan, F-33170 Gradignan, France

³⁷ IPHC, Université de Strasbourg, CNRS/IN2P3, F-67037 Strasbourg, France

³⁸ Aix Marseille Univ, CNRS/IN2P3, CPPM, Marseille, France

³⁹ SUBATECH, Université de Nantes, IMT Atlantique, CNRS-IN2P3, Nantes, France

⁴⁰ III. Physikalisches Institut B, RWTH Aachen University, Aachen, Germany

⁴¹ Institute of Experimental Physics, University of Hamburg, Hamburg, Germany

⁴² Forschungszentrum Jülich GmbH, Nuclear Physics Institute IKP-2, Jülich, Germany

⁴³ Institute of Physics and EC PRISMA⁺, Johannes Gutenberg Universität Mainz, Mainz, Germany

⁴⁴ Technische Universität München, München, Germany

⁴⁵ Helmholtzzentrum für Schwerionenforschung, Planckstrasse 1, D-64291 Darmstadt, Germany

⁴⁶ Eberhard Karls Universität Tübingen, Physikalisches Institut, Tübingen, Germany

⁴⁷ INFN Catania and Dipartimento di Fisica e Astronomia dell'Università di Catania, Catania, Italy

⁴⁸ Department of Physics and Earth Science, University of Ferrara and INFN Sezione di Ferrara, Ferrara, Italy

⁴⁹ INFN Sezione di Milano and Dipartimento di Fisica dell'Università di Milano, Milano, Italy

⁵⁰ INFN Milano Bicocca and University of Milano Bicocca, Milano, Italy

⁵¹ INFN Milano Bicocca and Politecnico di Milano, Milano, Italy

⁵² INFN Sezione di Padova, Padova, Italy

⁵³ Dipartimento di Fisica e Astronomia dell'Università di Padova and INFN Sezione di Padova, Padova, Italy

⁵⁴ INFN Sezione di Perugia and Dipartimento di Chimica, Biologia e Biotecnologie dell'Università di Perugia, Perugia, Italy

⁵⁵ Laboratori Nazionali di Frascati dell'INFN, Roma, Italy

⁵⁶ University of Roma Tre and INFN Sezione Roma Tre, Roma, Italy

⁵⁷ Pakistan Institute of Nuclear Science and Technology, Islamabad, Pakistan

⁵⁸ Joint Institute for Nuclear Research, Dubna, Russia

⁵⁹ Institute for Nuclear Research of the Russian Academy of Sciences, Moscow, Russia

⁶⁰ Lomonosov Moscow State University, Moscow, Russia

⁶¹ Comenius University Bratislava, Faculty of Mathematics, Physics and Informatics, Bratislava, Slovakia

⁶² High Energy Physics Research Unit, Faculty of Science, Chulalongkorn University, Bangkok, Thailand

⁶³ National Astronomical Research Institute of Thailand, Chiang Mai, Thailand

⁶⁴Suranaree University of Technology, Nakhon Ratchasima, Thailand

⁶⁵The University of Liverpool, Department of Physics, Oliver Lodge Laboratory, Oxford Str., Liverpool L69 7ZE, UK, United Kingdom

⁶⁶University of Warwick, University of Warwick, Coventry, CV4 7AL, United Kingdom

⁶⁷Department of Physics and Astronomy, University of California, Irvine, California, USA

Received: date / Accepted: date

^ae-mail: Juno_pub_comm@juno.ihep.ac.cn (corresponding author)

Abstract Large-scale organic liquid scintillator detectors are highly efficient in the detection of MeV-scale electron antineutrinos. These signal events can be detected through inverse beta decay on protons, which produce a positron accompanied by a neutron. A noteworthy background for antineutrinos coming from nuclear power reactors and from the depths of the Earth (geoneutrinos) is generated by (α, n) reactions. In organic liquid scintillator detectors, α particles emitted from intrinsic contaminants such as ^{238}U , ^{232}Th , and $^{210}\text{Pb}/^{210}\text{Po}$, can be captured on ^{13}C nuclei, followed by the emission of a MeV-scale neutron. Three distinct interaction mechanisms can produce prompt energy depositions preceding the delayed neutron capture, leading to a pair of events correlated in space and time within the detector. Thus, (α, n) reactions represent an indistinguishable background in liquid scintillator-based antineutrino detectors, where their expected rate and energy spectrum are typically evaluated via Monte Carlo simulations. This work presents results from the open-source SaG4n software, used to calculate the expected energy depositions from the neutron and any associated de-excitation products. Also simulated is a detailed detector response to these interactions, using a dedicated Geant4-based simulation software from the JUNO experiment. An expected measurable $^{13}\text{C}(\alpha, n)^{16}\text{O}$ event rate and reconstructed prompt energy spectrum with associated uncertainties, are presented in the context of JUNO, however, the methods and results are applicable and relevant to other organic liquid scintillator neutrino detectors.

Keywords Neutrino detectors, Liquid detectors, Models and simulations, Simulation methods and programs, Detector modelling and simulations

1 Introduction

Over the decades since the first experimental evidence of neutrino existence by Cowan and Reines in 1956 [1], liquid scintillator (LS) detectors have played a central role in neutrino physics. LS detectors of increasing size and improved performance have been developed, boasting broad physics programs. These detectors represent, so far, the only technology to detect reactor neutrinos at different baselines; in searches for sterile neutrinos (NEOS [2], STEREO [3], PROSPECT [4], DANSS [5]), measurement of neutrino oscillation parameters θ_{13} (Daya Bay [6], RENO [7], Double Chooz [8]), or the so-called *solar parameters* θ_{12} and Δm_{21}^2 (KamLAND [9]). The same detection technique has been exploited to measure geoneutrinos, as demonstrated by KamLAND [10] and Borexino [11]. Outside of antineutrino detection, Borexino has provided world-leading measurements of solar neutrinos, thanks to its unprecedented radio-purity [12]. SNO+ is also entering on the scene, with the primary goal to search for $0\nu\beta\beta$ decay [13], but also

to measure reactor and geoneutrinos [14]. JUNO [15, 16] is the first multi-kiloton LS detector, under construction in the South of China. Its design is driven by its main physics goal to determine the neutrino mass ordering [17], through precise measurement of the oscillation pattern in the energy spectrum of reactor neutrinos at a 52.5 km baseline.

Detection of reactor electron antineutrinos is made through the charged-current Inverse Beta Decay (IBD) reaction on protons:

$$\bar{\nu}_e + p \rightarrow e^+ + n. \quad (1)$$

IBD interactions feature a minimum antineutrino kinetic energy threshold of 1.8 MeV, corresponding to the mass difference between the emitted particles, namely the neutron n and positron e^+ , and the initial proton p . The products of this reaction, schematized in figure 1, yield a distinct coincident signal. The positron e^+ deposits its kinetic energy in the LS, then quickly annihilates with an electron in the detector, producing detectable scintillation light. This *prompt* signal bears information of the energy of the incident neutrino. The emitted neutron propagates on a random walk, quickly thermalizing via elastic collisions, typically with protons in the detector, until it is eventually captured by a proton/nucleus in the detector. Neutron capture on protons yields a deuteron followed by a 2.2 MeV γ . Neutrons can also be captured on ^{12}C in organic LS that leads to a 4.95 MeV γ emission. This option takes place with about 1% probability. The *delayed* event typically happens in LS with an averaged lifetime of roughly 200 μs , where its precise value depends on the exact LS composition. Moreover, if LS is doped with gadolinium, neutron captures predominantly occur on isotopes of this chemical element, the capture time is substantially reduced, and a series of γ s with a total energy of 8 MeV is emitted [18]. In any case, the capture usually happens tens of centimeters away from the IBD interaction point. The distinct prompt-delayed space and time coincidence is a powerful characteristic for the selection of antineutrino interactions.

In spite of the background suppression power of the IBD coincidence tag, several background categories pose important challenges in antineutrino detection. Cosmogenic or accidental coincidence pair backgrounds, for example, can be evaluated and constrained in analysis by exploiting independent data sets. This can be done by collecting the events following cosmogenic muons and using off-time windows in the search for IBD-like events, respectively. Another correlated background, which can mimic the IBD signal, is known as the (α, n) reaction, the focus of this work. In organic LS detectors, where there are large amounts of carbon, the dominant (α, n) reaction occurs on ^{13}C (with a natural abundance of 1.1% [19]). This produces ^{16}O , often in an excited state, alongside a MeV-scale neutron. Preceding the delayed neutron capture, prompt signals can be generated by inelastic

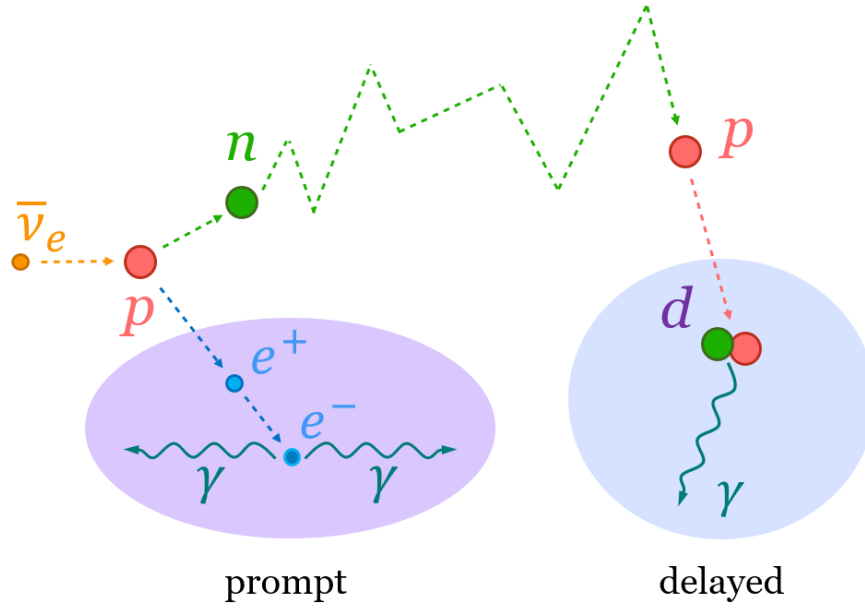


Fig. 1 Schematic of the IBD reaction on proton used for electron antineutrino detection in LS detectors. It demonstrates the origin of the prompt (violet area) and the delayed (blue area) signals, and underlines the similarity with the background caused by (α, n) reactions shown in figure 5.

scattering of the neutron, along with higher energy radiation emitted upon the de-excitation of ^{16}O , leading to correlated event pairs within the detector. Thus, the (α, n) reactions represent an indistinguishable background in LS-based antineutrino detection. It is worth noting that (α, n) reactions can also act as a background in direct searches for dark matter [20].

This work focuses on the evaluation of the (α, n) background, the prediction of which strongly relies on Monte Carlo (MC) simulations and cannot be evaluated from independent datasets. In several experiments, the principal α particle source assumed to produce (α, n) reactions, was ^{210}Po [9, 11, 14], but these reactions can also be sourced by α particles of various energies produced along the ^{238}U and ^{232}Th decay chains [21]. The relative contribution of different α -producing isotopes depends on the achieved radiopurity of the LS.

Presented here are results for the (α, n) background simulated in the JUNO experiment. First introduced is the JUNO detector in section 2. The assumed sources of α s in LS are detailed in section 3. The main characteristics of the $^{13}\text{C}(\alpha, n)^{16}\text{O}$ reactions and the generation mechanisms of the prompt and delayed signals are then described in section 4. $^{13}\text{C}(\alpha, n)^{16}\text{O}$ reactions are simulated in the LS target using SaG4n v1.3 software [22], presented in section 5, alongside the estimated interaction rates and neutron yields, with respective uncertainties. Products of the (α, n) reactions, which deposit energy in the LS predicted by SaG4n, are then input to the JUNO simulation software (JUNOSW) [23], implementing the full detector response

and event reconstruction, which is covered in section 6. Also presented in this section is the selection procedure of IBD-like events due to (α, n) reactions, and the final expected measurable spectral shapes. Section 7 summarises the expected IBD-like background event rates due to $^{13}\text{C}(\alpha, n)^{16}\text{O}$ reactions, based on expected natural radioactivity concentrations in JUNO, along with discussion of the various systematic uncertainties. Section 8 concludes the article and summarises the results, highlighting their possible applications and relevance to other organic LS-based neutrino detectors.

2 The JUNO detector

The Jiangmen Underground Neutrino Observatory (JUNO) experiment is a 20-kiloton LS detector in southern China in an underground laboratory with a vertical overburden of ≈ 650 m (1800 m.w.e.). JUNO's primary physics goal is to measure the neutrino mass ordering (NMO), by resolving the fine structure due to flavor oscillations in the antineutrino energy spectrum from nearby nuclear reactors. In order to achieve this precision measurement, the detector is expected to reach an unprecedented energy resolution of 3% at 1 MeV [24].

A sketch of the JUNO detector is shown in figure 2. It consists of a Central Detector (CD), containing 20 kt of LS in a 17.7 m radius acrylic sphere of 120 mm thickness. The acrylic vessel is supported by a spherical stainless steel (SS) structure via 590 connecting bars. The LS target is watched by 17,612 20-inch and 25,600 3-inch photomultiplier tubes (PMTs) mounted on the SS structure. This al-

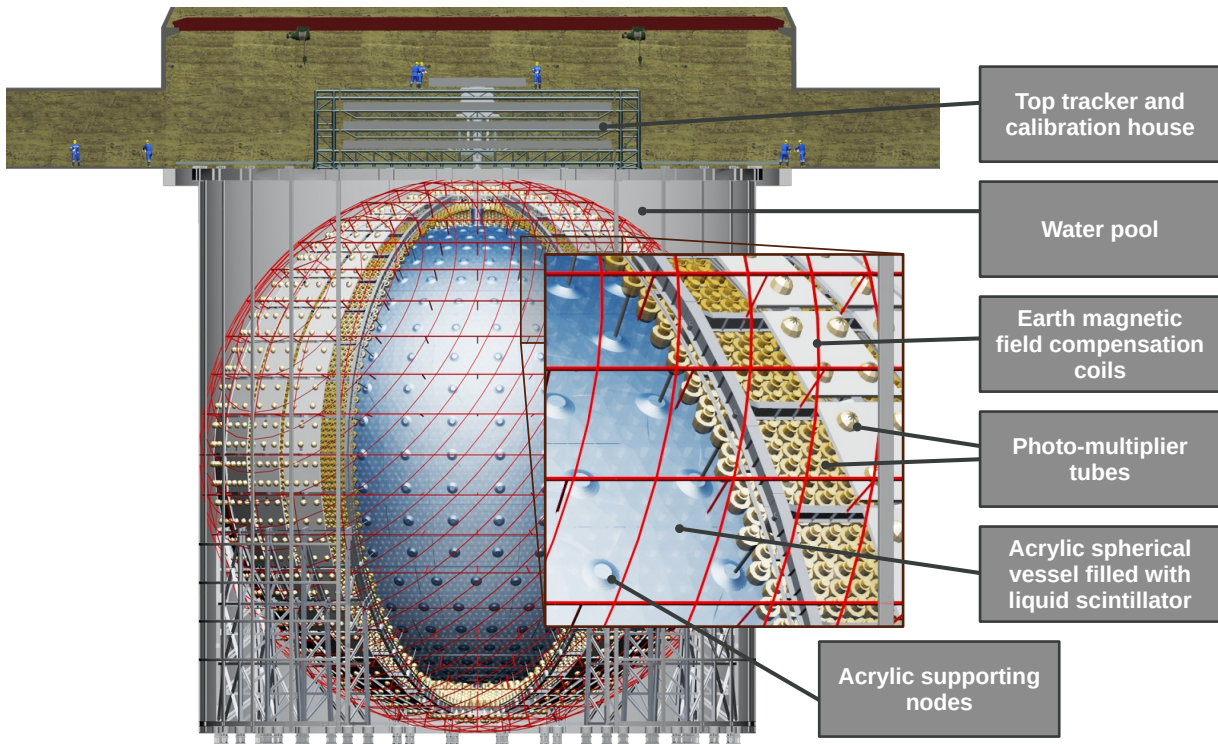


Fig. 2 Schematic drawing of the main JUNO detector.

lows for a first-rate photosensitive coverage (75.2% for the 20-inch and 2.7% for the 3-inch PMTs), which is needed to collect a large number of photoelectrons per unit of deposited energy in the scintillator.

The LS cocktail has been optimized in dedicated studies with the Daya Bay detector [26]. The LS is primarily made up of linear alkylbenzene (LAB), consisting of long alkyl chains and typically containing 10-16 C atoms with a benzene ring attached at the end. JUNO employs a primary fluor in the form of 2,5-Diphenyloxazole (PPO), at a concentration of 2.5 g/L, to avoid scintillation light re-absorption during its propagation within the detector. To increase the scintillation detection efficiency on PMTs, a wavelength shifter of p-bis-(o-methylstyryl)-benzene (bis-MSB) is also added at 3 mg/L. LAB and its associated fluors were selected due to its high light yield, good α/β particle discrimination [27], and the ability to reach very high levels of purity. This scintillation mixture expects to allow for light attenuation lengths greater than 20 m at 430 nm in order to make up for the huge CD dimensions. In order to boost light collection, and reduce the levels of aforementioned naturally occurring radioactivity within the LS, it is passed through optical and radiochemical purification [28]. A pre-detector (OSIRIS) also monitors 15% of the LS for its radioactive contamination levels prior to filling into the JUNO detector [29].

The CD is submerged in a cylindrical water pool (WP) of 43.5 m diameter and height of 44.0 m, filled with 35 kt of ultrapure water. The WP shields the CD against external fast

neutrons and γ s. It also acts as a Cherenkov veto for atmospheric muons, which have a flux of about $4 \times 10^{-3} \text{ m}^{-2} \text{ s}^{-1}$. Cherenkov light produced by muons passing through water can be detected by the 2,400 20-inch PMTs installed on the outer surface of SS structure. On the top of the WP, a Top Tracker (TT) is placed to precisely measure the tracks of a subsample of the crossing muons [30].

Multiple calibration systems implementing radioactive and laser-based sources have been developed to calibrate the detector and to evaluate the non-uniformity and non-linearity of its response. The employed radioactive sources include γ sources of various energies, a ^{68}Ge positron source, $^{241}\text{Am}-\text{Be}$ (AmBe) and $^{241}\text{Am}-^{13}\text{C}$ (AmC) neutron sources. Calibration operations will be carried out through a stainless steel chimney, which connects the CD to the outside from the top. Calibration sources can be deployed throughout the inside of the acrylic vessel using an Automatic Calibration Unit (ACU) [31], which covers the central axis, while the Cable Loop System (CLS) [32] allows for coverage of the off-axis region in a two-dimensional plane. A Guide Tube Calibration System (GTCS) [33] can place sources on the outer surface of the acrylic sphere. Details regarding the calibration systems and strategies can be found in [34].

JUNO's world-leading size, low backgrounds, and unprecedented energy resolution, allow for a very broad physics program, measuring neutrinos from various sources, ranging in energy from tens of keV to tens of GeV [15, 16]. Beyond reactor antineutrinos, JUNO will be able to detect

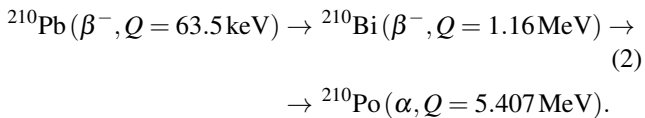
Table 1 Summary of α decaying isotopes from the ^{238}U and ^{232}Th chains in secular equilibrium, showing the respective half-lives $\tau_{1/2}$, α energies E_α , and branching ratios BR_α based on NuDAT [25]. Branches with BR_α less than 1% are not shown here but considered in the analysis and depicted in lower part of figure 4.

^{238}U chain				^{232}Th chain			
Parent	$\tau_{1/2}$	E_α [MeV]	BR_α [%]	Parent	$\tau_{1/2}$	E_α [MeV]	BR_α [%]
^{238}U	4.4×10^9 y	4.198	79.0	^{232}Th	1.4×10^{10} y	4.012	78.2
		4.151	20.9			3.947	21.7
^{234}U	2.4×10^5 y	4.774	71.38	^{228}Th	1.91 y	5.423	73.4
		4.722	28.42			5.340	26.0
^{230}Th	7.5×10^4 y	4.687	76.3	^{224}Ra	3.66 d	5.685	94.92
		4.620	23.4			5.448	5.06
^{226}Ra	1600 y	4.784	93.84	^{220}Rn	55 s	6.288	99.88
		4.601	6.16			6.778	99.99
^{222}Rn	3.82 d	5.489	99.92	^{212}Bi	61 min	6.089	9.74
^{218}Po	3.098 min	6.002	99.98			6.050	25.12
^{214}Po	164.3 μs	7.686	99.96	via ^{212}Po		8.784	64.06
^{210}Po	138.3 d	5.304	99.99	(3×10^{-7} s)			

solar, geo, atmospheric, and supernovae neutrinos, and to search for evidences of physics beyond the Standard Model (BSM) [16, 35–40].

3 Sources of α particles

Liquid scintillators employed in neutrino detectors undergo complex purification procedures, strongly reducing its radioactivity. Nevertheless, residual impurities do contain α emitting isotopes triggering $^{13}\text{C}(\alpha, n)^{16}\text{O}$ reaction. The most common source of α s was found to be ^{210}Po [9, 11, 14], the last radioactive isotope of ^{238}U chain, often breaking the secular equilibrium of the chain and contaminating the LS in much increased levels. Out-of-equilibrium ^{210}Po with half-life of 138.4 days can be brought to LS stand-alone from external materials due to its chemical properties and mobility [41]. ^{238}U chain secular equilibrium is often broken also by increased levels of relatively longed lived ^{210}Pb . With its 22-year half-life, ^{210}Pb represents a steady source of ^{210}Po in the LS, via



Moreover, ^{238}U chain also includes another long-lived nuclide, namely ^{226}Ra with 1600-year half-life, which is a source of ^{222}Rn and a series of short-lived daughters. The respective out-of-equilibrium component [20] might be present in the JUNO CD, if, for example, there is an air leak, usually containing a large amount of ^{222}Rn . This extra source of α particles can be easily identified by monitoring the rate of so-called Bi-Po events (see Sec. 7.2.1).

Liquid scintillators typically contain residual amounts of ^{238}U and ^{232}Th in secular equilibrium, in which decays

from all the daughter isotopes occur at the same rate. The α decaying isotopes, 8 from the ^{238}U and 6 from the ^{232}Th chains, produce, respectively, 12 and 11 α s, as summarized in table 1, showing the respective half-lives, α energies, and branching ratios from NuDAT [25]. The relative weights of different α s as a function of their energy in both chains are visualized in figure 3. We note, that decay modes with branching ratio less than 1% are not included for clarity here, though they were included in the simulation studies presented in this work and are shown in the lower part of figure 4 in a direct comparison with the $^{13}\text{C}(\alpha, n)^{16}\text{O}$ cross section.

The world’s best LS radiopurity was achieved by Borexino [42, 43], suppressing ^{238}U and ^{232}Th by ten orders of magnitude (less than 9.4×10^{-20} g/g of ^{238}U and less than 5.7×10^{-19} g/g of ^{232}Th at 95% C.L.). This level of radiopurity was fundamental for the successful detection of solar neutrinos via elastic scattering off electrons. In Borexino, out-of-equilibrium ^{210}Po was thus the only source of the overall almost negligible (α, n) background in the measurement of geoneutrinos [11]. Thanks to the IBD coincidence tag, experiments which focus on antineutrino detection do not require such extreme radiopurity levels. Nevertheless, the (α, n) background played an important role in KamLAND’s reactor [44] and geoneutrino measurements [10], especially in its first phase before additional LS purification. Recent reactor antineutrino measurements in SNO+ featured significant rates of ^{210}Po -sourced (α, n) , which proved to be the most significant background [14]. The Daya Bay experiment considered α decays from ^{210}Po , ^{238}U , ^{232}Th , and ^{227}Ac , however, due to the very high reactor signal flux, (α, n) was evaluated to occur at a negligible rate [21].

In this work, we evaluate the $^{13}\text{C}(\alpha, n)^{16}\text{O}$ background from ^{238}U and ^{232}Th chains, from out-of-equilibrium $^{210}\text{Pb}/^{210}\text{Po}$, and from unsupported ^{210}Po in JUNO. As the

final LS radiopurity is not yet known, we consider the minimum radiopurity level requested for the NMO measurement, that is, 10^{-15} g/g for ^{238}U and ^{232}Th . ^{210}Pb , which subsequently decays to ^{210}Po , can fall out of equilibrium from the ^{238}U chain, and is evaluated to be 5×10^{-23} g/g relying on JUNO's radioactivity control strategy [36, 45]. The contamination from unsupported ^{210}Po is 3×10^{-22} g/g, based on a ^{210}Po rate of 8×10^4 cpd/kt ("cpd" stands for counts per day) reported in Borexino as the average value in the whole LS volume at the beginning of data taking [11]. It is reasonable to assume that this initial contamination originated from the inner surfaces of the LS filling system and the target vessel. We assume the same contamination level of the surfaces in JUNO as in Borexino, accounting for differences in surface areas and LS volumes. The ^{227}Ac α source, observed in the Daya Bay measurement, is not expected to have significant presence in JUNO and is therefore not considered in this work. The ^{235}U decay chain, of which ^{227}Ac is a daughter isotope, has a natural abundance of less than 1%. The heightened concentration of ^{227}Ac seen in Daya Bay was determined to originate from the Gd loaded in their LS, which will not be added to the JUNO LS cocktail during the NMO-measurement phase.

4 $^{13}\text{C}(\alpha, n)^{16}\text{O}$ reaction in liquid scintillator

The cross-section which quantifies the probability of a $^{13}\text{C}(\alpha, n)^{16}\text{O}$ reaction occurring for a given incident α particle energy, used in this work, is shown in the top part of figure 4. These data are adopted from the JENDL/AN-2005 data library [46], implemented in SaG4n package as the only available evaluation of the (α, n) reactions cross-sections, which was calculated based on experimental data. The data points in the top plot of figure 4 show multiple resonances, which is expected for (α, n) reactions on light nuclides, such as ^{13}C . This dependence is due to the complex mechanism of formation of a compound nucleus, which has numerous energy levels for possible excited states. The lower part of figure 4 shows the complete α spectra from ^{238}U and ^{232}Th chains, including branches with BR_α below 1%, that were not explicitly discussed in the previous section, but considered in the analysis. It can be seen that α particle energies extend from around 3.5 MeV to 9 MeV.

There are three distinct mechanisms by which the $^{13}\text{C}(\alpha, n)^{16}\text{O}$ reaction can mimic an IBD coincidence pair, schematized and labeled in figure 5. In each case, a neutron is emitted, producing an identical *delayed* neutron capture event. The basic scenarios of the prompt formation can be described as follows:

1. **Prompt-I from scattered protons:** The emitted neutron elastically scatters multiple protons within the first $\mathcal{O}(\text{ns})$ of its random walk, producing scintillation light.

2. **Prompt-II from $^{16}\text{O}^*$ de-excitation:** Upon the capture of an α particle with a kinetic energy above ~ 5 MeV, ^{16}O may be produced in an excited state. For the first excited state, n_1 , during de-excitation, a pair of $e^+ + e^-$ is emitted with a total kinetic energy of 5.03 MeV. The annihilation of the positron with an electron in the detector yields γ s of total energy 1.02 MeV, resulting in a prompt event with a total deposited energy of 6.05 MeV. In the cases ^{16}O is produced in its 2nd, 3rd, and 4th excited states, n_2 , n_3 , and n_4 , transitions to the ground state release γ s with energies 6.130 MeV, 6.917 MeV, and 7.117 MeV, respectively, as seen in figure 6.

3. **Prompt-III from $^{12}\text{C}^*$ de-excitation:** ^{16}O is produced in its ground state, but the high energy neutron inelastically scatters off a ^{12}C nucleus, prompting its excitation and subsequent emission of a 4.4 MeV γ .

We note that the proton scattering, described in Prompt-I, also occurs in coincidence with the Prompt-II and Prompt-III mechanisms. In these cases, however, the available energy for the neutron has already been used in the excitation of either ^{16}O or ^{12}C , where proton scattering causes emission of only a small amount of scintillation light.

We also note that the α particle deposits a fraction of its initial kinetic energy into the LS before its capture on ^{13}C . Furthermore, the quenching effect strongly decreases the visible energy produced by α s, typically by an order of magnitude compared to $e^{+/-}$ and γ s. Consequently, the α s yield small but measurable scintillation light which combines with each of the prompt processes described above.

Overall, $^{13}\text{C}(\alpha, n)^{16}\text{O}$ reaction can produce IBD-like coincident signals with prompt energies up to about 7 MeV, featuring a complex energy spectrum. The following section describes the simulation of $^{13}\text{C}(\alpha, n)^{16}\text{O}$ reactions in LS using the SaG4n tool.

5 Simulation of the $^{13}\text{C}(\alpha, n)^{16}\text{O}$ reaction in liquid scintillator

The first step in the evaluation of an IBD-like background from $^{13}\text{C}(\alpha, n)^{16}\text{O}$ reaction is its simulation using the Geant4-based simulation tool SaG4n [22]. SaG4n package version 1.3 with Geant4.11.1.2 [47–49] was used in this work. Taking into account the incident α s of different energies from expected radio-impurities, we simulate the energy loss by α s in the LS until its eventual capture on ^{13}C nuclei, accounting for the cross-sectional energy dependence. Several cross-section libraries are available within the program. We adopted the JENDLTENDL01 dataset, since it contains the aforementioned JENDL/AN-2005 cross section evaluations for capture on carbon. In section 5.1 we describe our inputs and settings used in the SaG4n software, which can in general be used to simulate various (α, n) reactions in different materials. Section 5.2 describes simulation results in

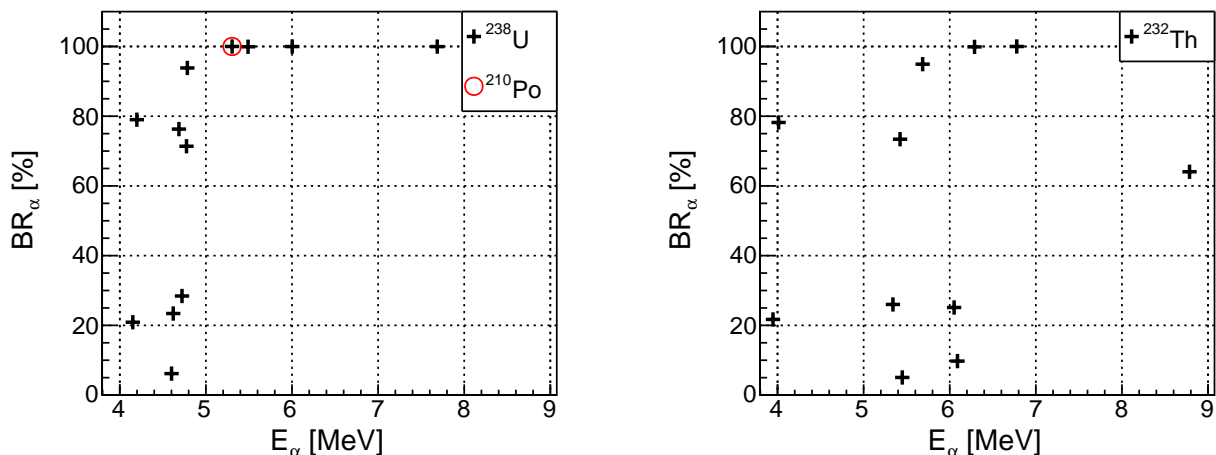


Fig. 3 The branching ratios of α particles from the ^{238}U (left) and ^{232}Th (right) radioactive chains in secular equilibrium (see also table 1) are shown as a function of α energy. The α from ^{210}Po , often breaking the equilibrium of the ^{238}U chain, is marked with a red circle in the left figure.

terms of the branching ratios of different energy levels of the produced ^{16}O nucleus, neutron yields, and neutron energy spectra. In section 5.3 we discuss various systematic effects that can impact our conclusions.

5.1 SaG4n software settings and inputs

SaG4n requires definition of the target material composition and geometry, sources of α s, and of several parameters characterizing the simulation process. We simulated the (α, n) reaction as well as the de-excitation of the ^{16}O nucleus, while all secondary particles are disabled. In this work, we have used the following definitions:

- ALPHA SOURCES: We simulated 2×10^9 decays of ^{210}Po and the same number of alphas from ^{238}U and ^{232}Th chains in secular equilibrium. For the latter two, we used built-in SaG4n functions to provide the energies and relative intensities of each α decay within these chains, as seen in the lower part of figure 4. All α s are emitted isotropically within a cube of 10 cm side length placed in the center of the simulated target.
- TARGET GEOMETRY: A cube of 100 cm side length, sufficiently large with respect to the size of the α sources and mm range of α s, guaranteed full energy deposition in the target.
- TARGET MATERIAL: JUNO LS was characterized with a simplified chemical formula $\text{C}_6\text{H}_5\text{C}_{14}\text{H}_{29}$ and with a density of 0.853 g/cm^3 at 20°C . The corresponding mass fractions of hydrogen and carbon are 12.49% and 87.51%, respectively. Since the scintillator cocktail consist of 99.7% LAB by mass, there is assumed negligible impact of the C nuclei present from the PPO and

bis-MSB fluors. A natural abundance of ^{13}C equal to $\sim 1.1\%$ [19] was considered.

- SIMULATION PARAMETERS: The SaG4n parameter named the *bias factor* allows one to magnify the α capture cross section in the material in order to reduce the computing time for the simulation of a desired number of events. Consequently, reaction products are generated with weights ω , which take into account the enhancement of the (α, n) cross section. A bias factor of 10^4 was assumed in this work. It was found that there was negligible impact to results when bias factors of 10^5 or 10^6 were used. Another important parameter is the *maximum allowed step length* (S_{max}) for the propagation of α particles within the material. The chosen step length, unless stated otherwise, was $1 \mu\text{m}$, a factor of 10 smaller than SaG4n's default value. This choice is discussed in section 5.3.

5.2 Reaction products

SaG4n outputs information about all energy-depositing particles involved in the (α, n) reaction. For each simulated interaction, we recorded the energy, position, and direction of α at emission and capture on ^{13}C as well as of the neutron and ^{16}O de-excitation product(s).

The neutron yield $Y[n/\alpha]$ in SaG4n simulation, *i.e.* the probability per α to trigger a $^{13}\text{C}(\alpha, n)^{16}\text{O}$ reaction, can be defined as:

$$Y[n/\alpha] = \frac{1}{N_\alpha} \sum_{i=1}^{N_n} \omega_i, \quad (3)$$

where N_n is the total number of neutrons produced in simulation, ω_i is the weight of each neutron event, and N_α is

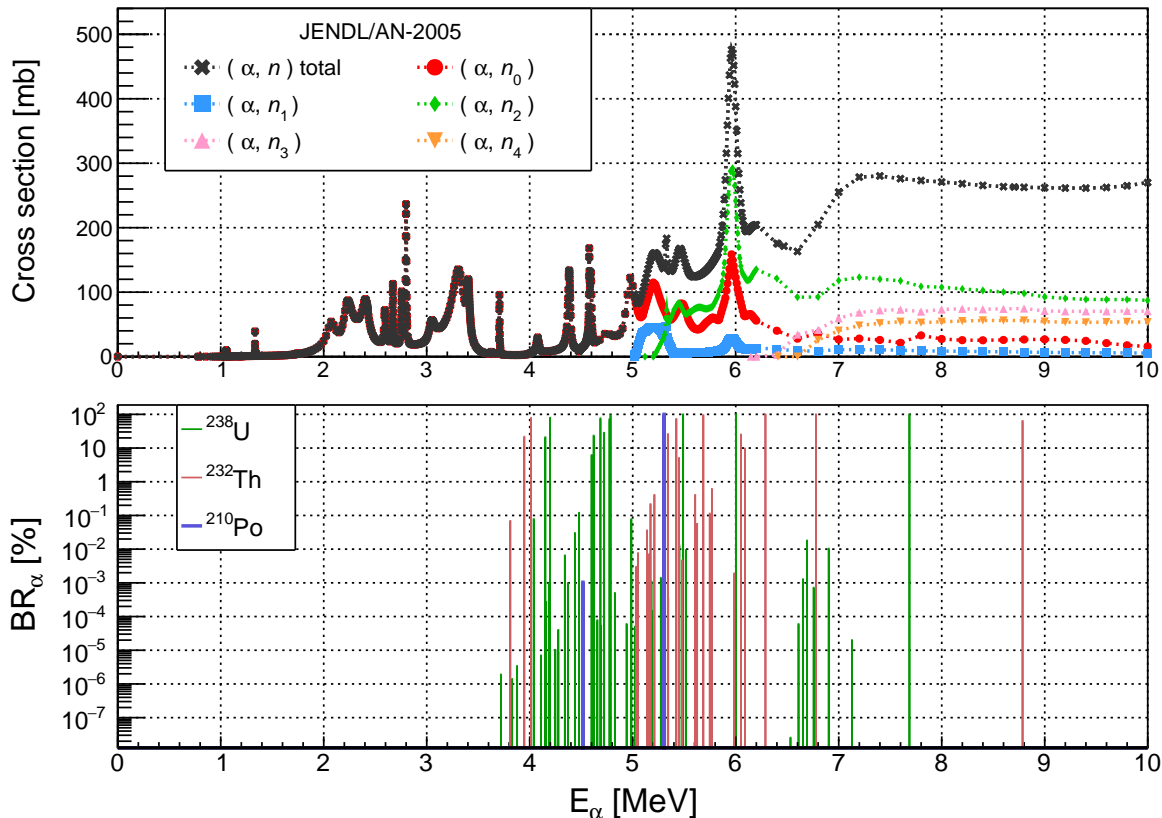


Fig. 4 Top: Values of the $^{13}\text{C}(\alpha, n)^{16}\text{O}$ reaction cross-section as a function of the initial α energy are taken from the JENDL/AN-2005 data library [46] and shown with different markers for the considered excitation levels of oxygen. The total cross section is shown in black; note that below 5 MeV this overlaps with red markers of the cross section for the case when ^{16}O is created in the ground state n_0 . The other colours mark the partial cross sections of the cases when ^{16}O is produced in excited states up to n_4 . Dotted lines connecting data points are to only guide the eye. Bottom: The complete α spectra from ^{238}U and ^{232}Th chains assuming secular equilibrium and from ^{210}Po decay, used in this study.

the number of simulated initial α particles. For radioactive chains, we define neutron yield of the whole chain in secular equilibrium, $Y[n/\text{chain}]$, that is obtained by multiplying the $Y[n/\alpha]$ by the number of α -decaying isotopes in each chain, e.g. 8 for ^{238}U and 6 for ^{232}Th .

Results from the simulation of ^{210}Po are shown in figure 7. The 5.3 MeV α allows population of not only the ground state but also of the 1st and 2nd excited states of ^{16}O . The energy spectrum of de-excitation e^+e^- pairs at 6.049 MeV and γ s at 6.130 MeV can be seen in the left plot of figure 7. The right part of this figure demonstrates the correlation between the energy of emitted neutron and the deposited energy of α particle prior to its capture. When ^{16}O is produced in its ground state, the emitted neutron acquires energies in the range of 3 to 7 MeV and energy depositions from the α can extend up to about 4.5 MeV. The horizontal bands clearly visible in the figure correspond to the fine structure in the α capture cross section, as shown in the top part of figure 4. Thus, as the α decreases in energy, the probability of its capture can increase by a factor of more than 100 at certain energies. When ^{16}O is produced

in an excited state, most of the α energy is absorbed in the excitation itself. In these cases, the α deposits only a small amount of energy before its capture (well below 0.5 MeV) and only similar amounts of energy are transferred to the emitted neutron.

Figures 8 and 9 show final states from the simulation of $^{13}\text{C}(\alpha, n)^{16}\text{O}$ reactions triggered by α s from the ^{238}U and ^{232}Th chains in secular equilibrium, respectively. The complexity of the results is due to the extended number of emitted α s of different energies in each of the decay chains.

Numerical results regarding branching ratios of the energy levels of ^{16}O and neutron yields $Y[n/\alpha]$ and $Y[n/\text{chain}]$ for ^{210}Po , and the ^{238}U and ^{232}Th chains are summarized in table 2.

5.3 Systematic effects

Major systematic effects influencing the precision of our simulation of the $^{13}\text{C}(\alpha, n)^{16}\text{O}$ reaction are the cross section uncertainties, comparison of our results on neutron yield to

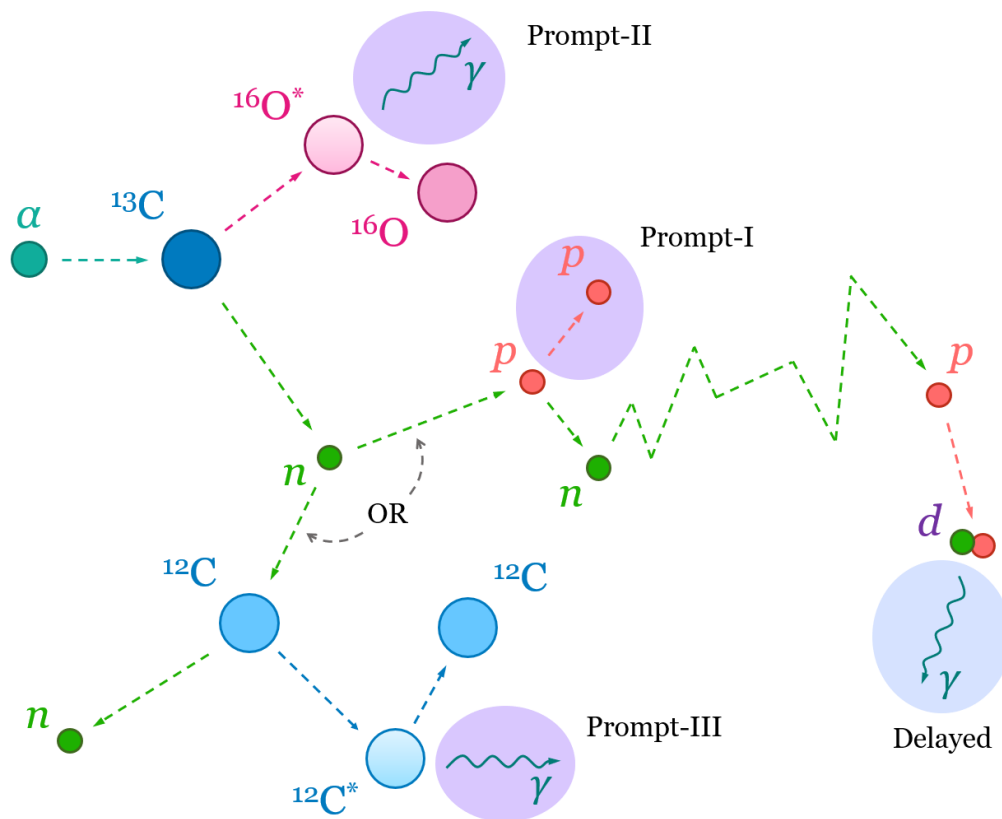


Fig. 5 Scheme of the (α, n) reaction on ^{13}C . The three processes that can generate the three kinds of the prompt signals, Prompt-I, II, and III, as described in text, are shown in violet areas. The blue area indicates the delayed signal from the neutron capture.

Table 2 Neutron yields and branching ratios (BR) of the populated ^{16}O nucleus states from SaG4n simulations.

chain or α source	BR [%]					$Y [n/\alpha]$	α/chain	$Y [n/\text{chain}]$
	n_0	n_1	n_2	n_3	n_4			
^{210}Po	89.3	9.3	1.4	0.0	0.0	5.11×10^{-8}	1	5.11×10^{-8}
^{238}U	51.5	7.9	29.3	7.0	4.3	7.95×10^{-8}	8	6.36×10^{-7}
^{232}Th	43.9	8.5	34.2	8.1	5.3	1.43×10^{-7}	6	8.58×10^{-7}

SaG4n reference, and the choice of non-physical parameters assumed in the simulations. They are discussed in this section.

Alpha capture cross section

The developers of the SaG4n software provided a comparison of the neutron yield from SaG4n to several calculation tools and nuclear data libraries for (α, n) reactions. Their tests covered more than 10 types of target materials including pure carbon, using ^{235}U , ^{238}U , and ^{232}Th decay chains as the α sources. The conclusion was that the neutron yields obtained with the SaG4n code and the JENDL/AN-2005 data library agreed with the experimental data within about 1% for carbon and better than 10% in most other cases [22].

In 2018, Mohr re-evaluated the $^{13}\text{C}(\alpha, n)^{16}\text{O}$ cross sections in the α energy region from 5 to 8 MeV [50], based on the capture data taken up to 8 MeV from Harissopoulos *et al.* [51]. Mohr proposed an average uncertainty of about 15% in the cross section up to 8 MeV in α energy.

Figure 10 shows the $^{13}\text{C}(\alpha, n)^{16}\text{O}$ cross sections as evaluated by Mohr and those available in the JENDL/AN-2005 library used in this work. The observed small discrepancy is mainly due to the use of different experimental data. However, thanks to the relatively close agreement of the curves in figure 10, the total cross-sectional uncertainty of 15% determined by Mohr was assumed to be the uncertainty in the neutron yield calculations using SaG4n.

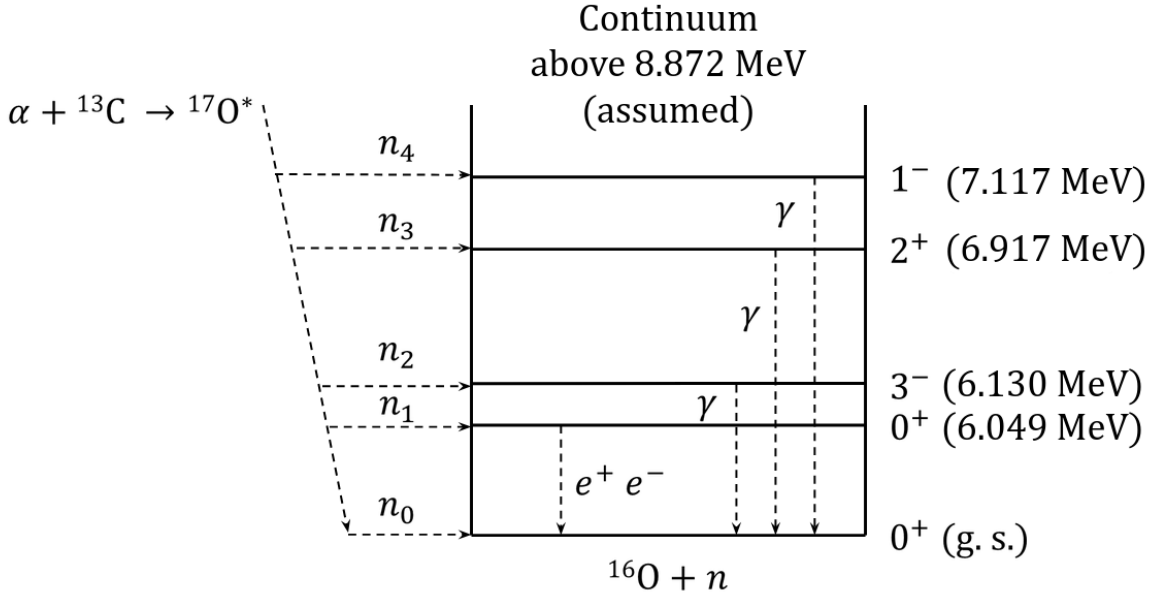


Fig. 6 The simplified level scheme of ^{16}O as populated in the $^{13}\text{C}(\alpha, n)^{16}\text{O}$ reaction [25]. Values n_0, n_1, n_2, n_3, n_4 represent which final state in ^{16}O is populated.

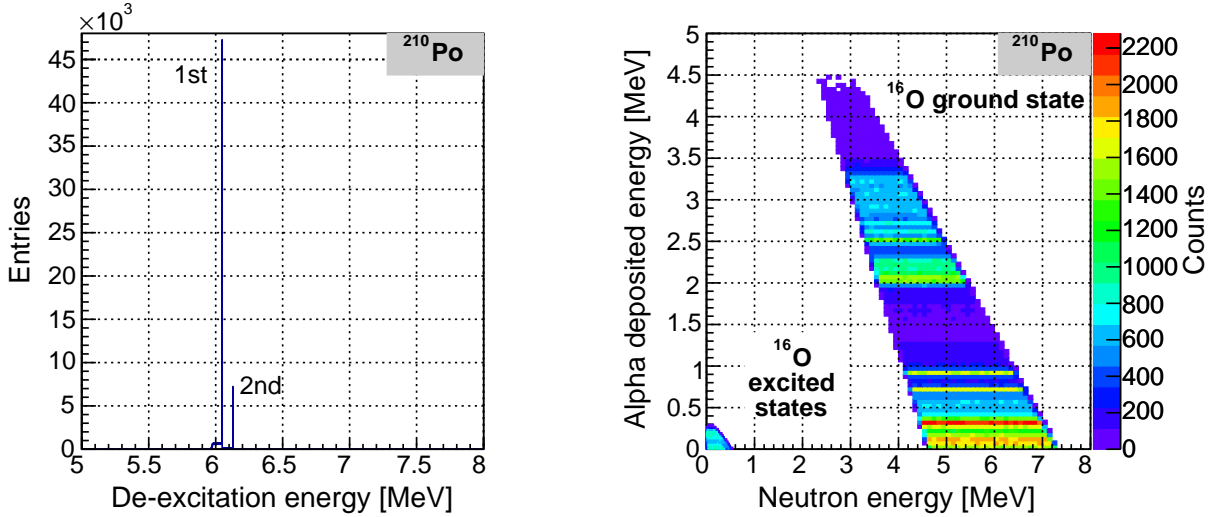


Fig. 7 SaG4n simulation of the $^{13}\text{C}(\alpha, n)^{16}\text{O}$ reaction in the JUNO LS triggered by 5.3 MeV α from ^{210}Po . Left: spectrum of e^+e^- pairs and γ s from de-excitation of the first and second ^{16}O excited states, respectively. Right: correlation between the energy of emitted neutron and deposited energy of the α particle prior to its capture.

Comparison to SaG4n reference neutron yields

The developers of SaG4n provided reference values of neutron yields from (α, n) reactions, using ^{235}U , ^{238}U , and ^{232}Th decay chains as the α sources, based on experimental data and their calculations [22]. The reference point on pure carbon target can be used to evaluate the precision of the neutron yields from this work. We repeated our calculations for targets with different hydrogen mass fractions in the range from zero (pure carbon target) to 50%, while keeping the density of 0.853 g/cm^3 . Stated previously, the target

representing the JUNO LS assumed a hydrogen mass fraction of 12.49%.

Figure 11 compares our results for the ^{238}U chain with different reference points. The neutron yields obtained with SaG4n software version 1.3, using the JENDL/AN-2005 data library, are shown for the LAB evaluation (black open circle) and for the variable hydrogen mass fractions (black full circles). We also show the pure-carbon reference values provided by SaG4n developers based on calculations with SaG4n v1.0 and JENDL/AN-2005 (blue cross) and from measurements (red cross). While the two reference points

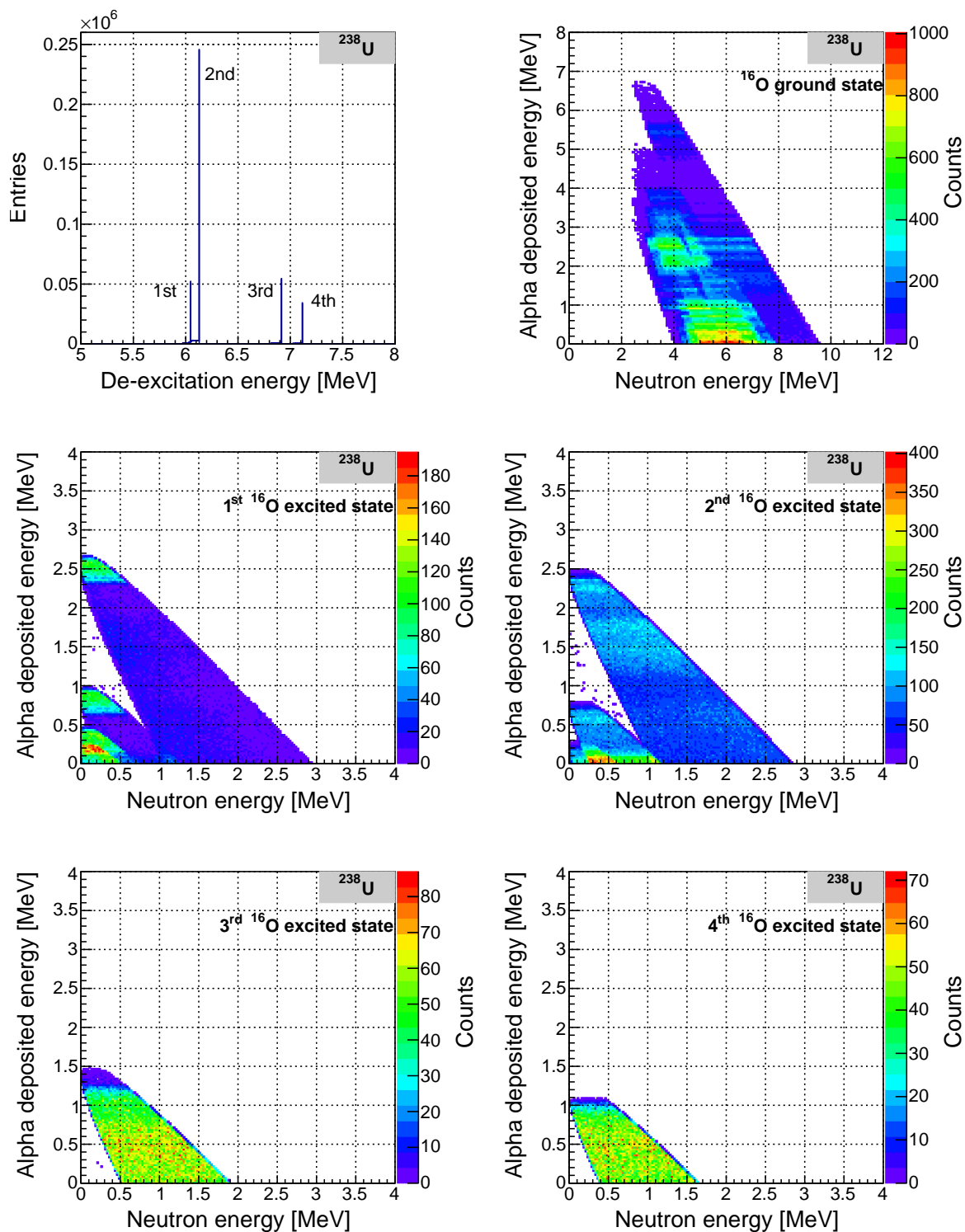


Fig. 8 SaG4n simulation of the $^{13}\text{C}(\alpha, n)^{16}\text{O}$ reaction in the JUNO LS triggered by α s from the ^{238}U chain in secular equilibrium. Top left: spectrum of e^+e^- pairs and γ s from de-excitation of the 1st and 2nd to 4th ^{16}O excited states, respectively. Other plots show correlations between the energy of emitted neutron and the deposited energy of α particle prior to its capture: top right plot for the case when ^{16}O is created in its ground state, while the remaining plots for the cases of the 1st to 4th ^{16}O excited states, respectively.

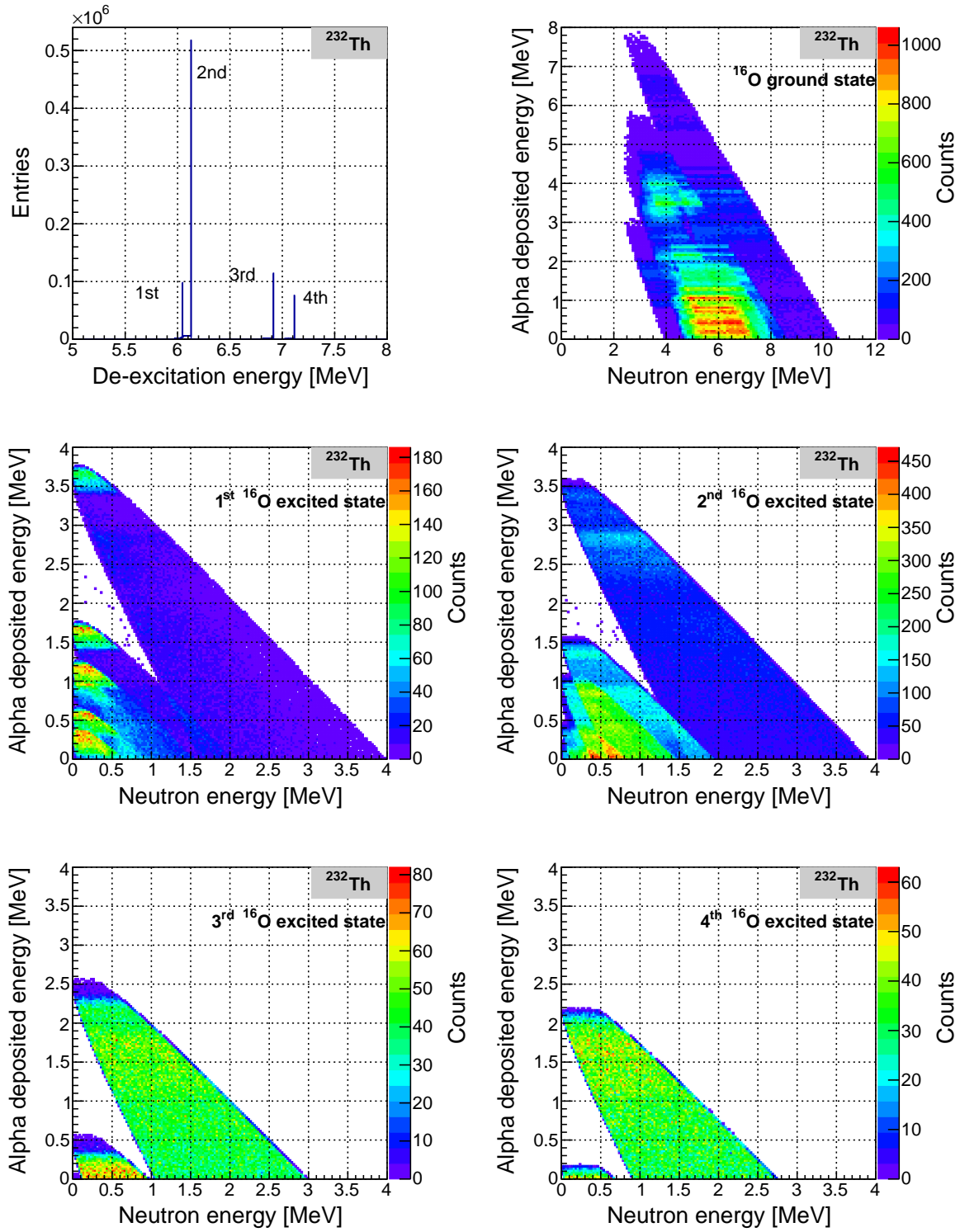


Fig. 9 SaG4n simulation of the $^{13}\text{C}(\alpha, n)^{16}\text{O}$ reaction in the JUNO LS triggered by α s from the ^{232}Th chain in secular equilibrium. Top left: spectrum of e^+e^- pairs and γ s from de-excitation of the 1st and 2nd to 4th ^{16}O excited states, respectively. Other plots show correlations between the energy of emitted neutron and the deposited energy of α particle prior to its capture: top right plot for the case when ^{16}O is created in its ground state, while the remaining plots for the cases of the 1st to 4th ^{16}O excited states, respectively.

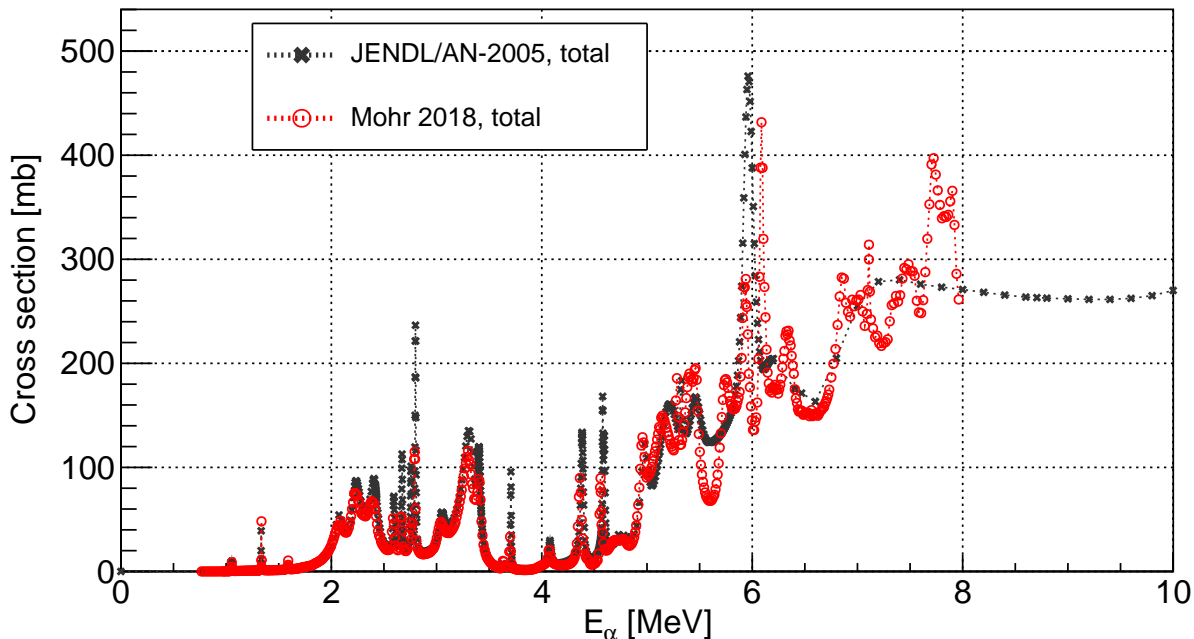


Fig. 10 Cross section of the $^{13}\text{C}(\alpha, n)^{16}\text{O}$ reaction as a function of α 's initial energy. Red markers (circles) show the cross section used in this work, as implemented in SaG4n from the JENDL/AN-2005 data library and shown also in figure 4. Black x-markers represent the re-evaluation by Mohr in 2018 [50], based on a 2005 experimental data set from Harissopoulos et al. [51].

are in agreement, a discrepancy of $\sim 18\%$ can be seen with respect to our pure-carbon evaluation. The corresponding level of agreement for ^{232}Th source was found to be 13%.

For further comparison, simulations were also run using the NeuCBOT calculation framework [20, 52, 53]. It can utilize the identical JENDL/AN-2005 cross-section database used in the SaG4n simulations. Two green triangle markers represent the ^{238}U NeuCBOT results for a pure-carbon material as well as for LAB. Our calculations with NeuCBOT and SaG4n are consistent at the level of 10% for ^{238}U and 5% for ^{232}Th .

The leading reason for these discrepancies was found to be due to the Geant4 version used during simulations. This work implemented the latest SaG4n software version 1.3, which was compiled with Geant4.11.1.2. The two reference values from the SaG4n article [22] were based on SaG4n software version 1.0, which was compiled with a modified version of Geant4.10.4.p01, and experimental data taken from [54], respectively. When we performed calculations with the older SaG4n version 1.1 and Geant4.10.05.p01, recommended by the authors, the yield difference compared to the original reference calculated yield (red marker), reduced to 8%. This work assumes the latest software versions available at the time of writing. To account for the differences in yields between our latest results and the available experimental reference data, a systematic error of 18% was assigned.

Maximum allowed step length for α simulation

The maximum allowed step length S_{\max} of a simulated α in SaG4n (section 5.1) was derived from the G4UserLimits class of the Geant4 standard library. Smaller values of S_{\max} lead to more detailed tracking of the propagation of α particles, allowing for more precision on the yields, at the expense of longer computation times. A study of the optimal S_{\max} in the JUNO LS target was carried out by scanning the range of S_{\max} from 10^{-8} m to 10^{-5} m, assuming ^{210}Po as well as ^{238}U and ^{232}Th chains as the α sources. Figure 12 shows the dependence of the neutron yield on the α step length. It can be seen that below $S_{\max} = 10^{-6}$ m, the yield approaches a stable value, within statistical fluctuations. Based on these studies, a value of $S_{\max} = 10^{-6}$ m was assigned for the simulation results shown in this work. Regarding the impact of the α step length on the systematic uncertainty on the neutron yield, a 5% value was assigned to reflect the fluctuations in the neutron yield seen for S_{\max} smaller than 10^{-6} m, for all three α sources.

6 JUNO detector response to $^{13}\text{C}(\alpha, n)^{16}\text{O}$

In this section, we discuss simulation of the JUNO detector's response to the products of $^{13}\text{C}(\alpha, n)^{16}\text{O}$ reactions,

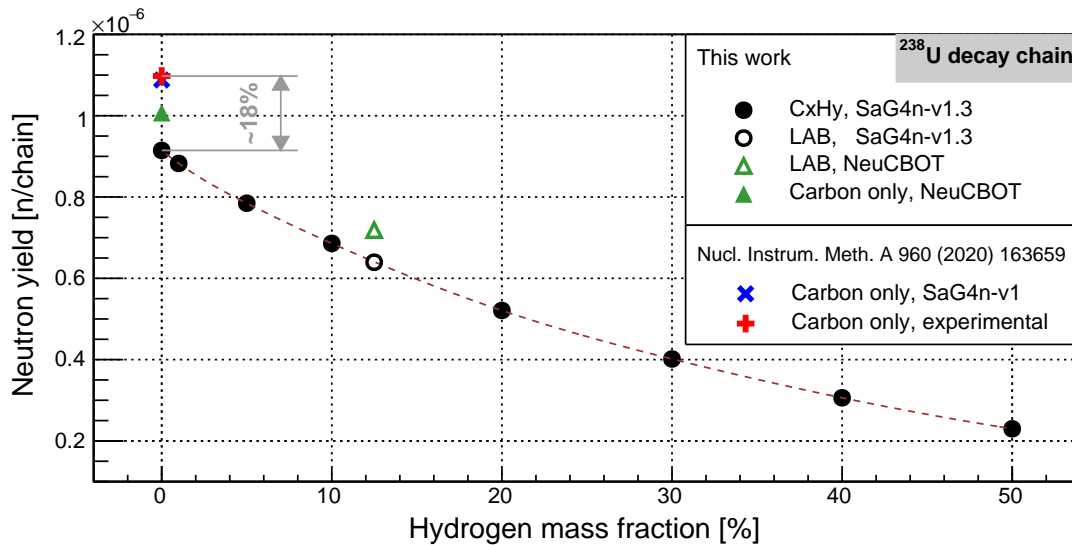


Fig. 11 Neutron yield as a function of hydrogen mass fraction in the target material for the $^{13}\text{C}(\alpha, n)^{16}\text{O}$ reaction, using the ^{238}U decay chain as the α source. The black circles represent the results obtained with the tools utilized in this study: SaG4n v1.3 plus JENDL/AN-2005 with Geant4.11.1.2. The black open circle corresponds to the respective yield for JUNO LAB. For comparison, calculations using the NeuCBOT framework with the JENDL/AN-2005 library are shown for the JUNO LAB case (green open triangle) and for pure carbon (green full triangle). The reference points taken from SaG4n developers [22] for SaG4n v1.0 plus JENDL/AN-2005 with Geant4.10.4.p01 and for experimental data are shown in blue and red crosses, respectively. A deviation of approximately 18% can be seen between the SaG4n result from this work and the only available experimental reference value for pure carbon.

described in the previous section. The JUNO collaboration has developed a dedicated Geant4-based software for detector performance studies, named JUNOSW [23]. This package reflects a detailed detector geometry and models particle energy depositions, light production including non-linear quenching effects, light propagation, as well as the response of PMTs [55, 56] and readout electronics. JUNOSW also includes event energy and vertex reconstruction algorithms. Further details regarding simulation and the reconstruction algorithms can be found in [24].

Section 6.1 describes the interface between SaG4n and JUNOSW. The following section 6.2 treats coincident event selection identically to that used in the IBD event search in previous JUNO reactor antineutrino sensitivity studies [17, 57]. In section 6.3 we finally present the spectral shapes of the IBD-like background due to the $^{13}\text{C}(\alpha, n)^{16}\text{O}$ reaction expected in JUNO.

6.1 SaG4n-JUNOSW interface

To simulate the detector response to $^{13}\text{C}(\alpha, n)^{16}\text{O}$ events inside the JUNO LS, SaG4n outputs (section 5.2) were used to determine the initial particles with respective energies to be simulated with the JUNOSW. These particles include any products of the ^{16}O de-excitation, either γ s or the e^+e^- pair, and the emitted neutron. For simulation of α particles, which deposit only part of their initial energy in the LS be-

fore the capture (E_{dep}), we apply an approximation that takes into account the energy dependence of the quenching effect in LS. The amount of emitted scintillation light for the same E_{dep} depends on the kinetic energy of α particle. Thus, we simulate the α with kinetic energy E_{gen} , depositing all of its energy in LS chosen such, that the same amount of light would be produced as if the source α of higher energy would deposit E_{dep} . As the amount of scintillation light emitted by the α prior to its capture is relatively small, this approximation was deemed appropriate.

All initial particles in the JUNOSW are isotropically generated from a single vertex, except the e^+e^- pair. Setting a random direction for the electron, we simultaneously impose an additional requirement for particles in the pair that they have opposite directions. The assumption of isotropy is acceptable for several reasons. Firstly, the (α, n) reaction and de-excitation of daughter nucleus are independent processes. Secondly, the outgoing neutron has some angular distribution with respect to the α particle direction at the moment of the reaction, but we can neglect this fact in our study, because when generating many events, the neutron directions in the JUNO LS target become equally probable on average. And finally, as for α s, that have kinetic energies below 10 MeV, they only propagate in LS up to $\sim 100 \mu\text{m}$ within 10 ps, which is negligible compared to ns-scale of the scintillation light emission.

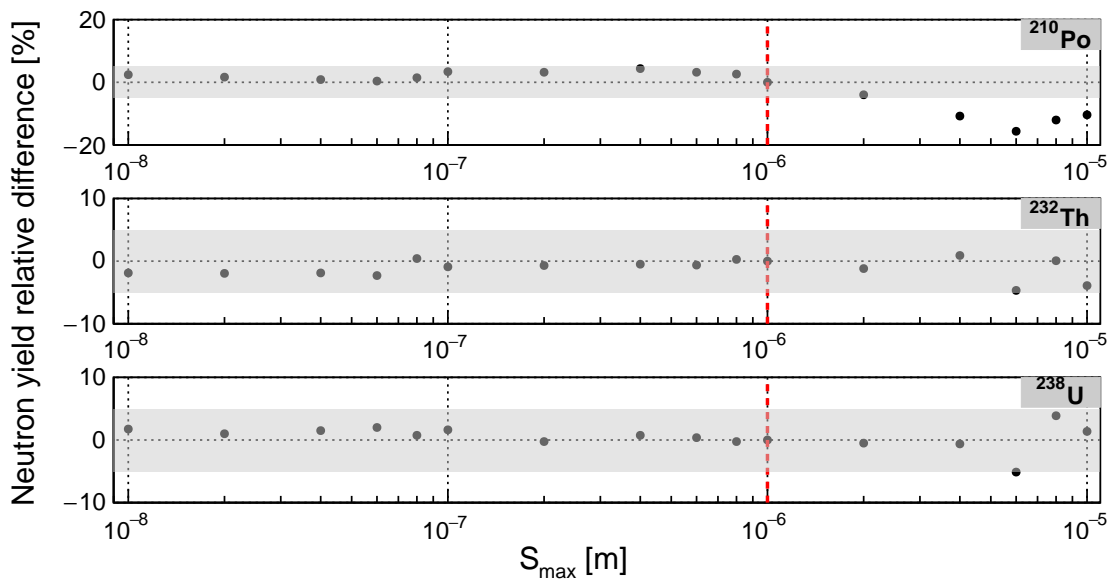


Fig. 12 Dependence of the neutron yield from $^{13}\text{C}(\alpha, n)^{16}\text{O}$ reaction on the maximum allowed step length S_{max} applied in the simulation of α particles with SaG4n. Y-axis shows relative differences with respect to the value of 10^{-6} m used in this work and marked by the vertical red dashed line. The three different graphs show the results for ^{210}Po (top) and for the ^{232}Th (middle) and ^{238}U (bottom) chains. The three horizontal shaded areas represent the assigned $\pm 5\%$ systematic uncertainty due to S_{max} .

6.2 IBD coincident event selection

For the next step in the evaluation of backgrounds from the $^{13}\text{C}(\alpha, n)^{16}\text{O}$ reaction expected in JUNO, we analyse simulation results from JUNOSW after event reconstruction. We perform coincident event selection, same to the one used in the IBD event search in the reactor antineutrino analyses of JUNO [17, 57], namely we apply the following cuts:

- prompt-delayed time difference: $dT < 1$ ms;
- prompt-delayed vertex distance: $dL < 1.5$ m;
- radial fiducial volume cut on the prompt vertex:
 $R_p < 17.2$ m;
- prompt reconstructed energy: $E_p \in (0.7, 12.0)$ MeV;
- delayed reconstructed energy: $E_d \in (1.9, 2.5)$ MeV or $E_d \in (4.4, 5.5)$ MeV.

The efficiency $\mathcal{E}_{(\alpha, n)}^{\text{IBD}}$ of these cuts is 0.84 for the ^{238}U and ^{232}Th chains and 0.87 for ^{210}Po . The unequal efficiencies reflect the different energies of the respective $^{16}\text{O}^*$ de-excitation products, also having different propagation ranges in the LS, as it will be shown in the next section.

It is worth noting that the used criteria may be tuned, or their set might even be partly changed in the further analyses, which will be based on the collected data.

6.3 $^{13}\text{C}(\alpha, n)^{16}\text{O}$ reconstructed energy spectra

The reconstructed energy spectra E_p representing the background in the antineutrino analysis are shown in the left column of figure 13 for the ^{238}U and ^{232}Th chains and ^{210}Po .

Different structures seen in these spectra represent the three different mechanisms described in Sec. 4 and in figure 5. In all three spectra, the broad peak below ~ 4 MeV reconstructed energy is due to protons scattered by neutrons (Prompt-I). All other more narrow peaks are due to the de-excitation of nuclei. The peaks above ~ 6 MeV are de-excitation products of $^{16}\text{O}^*$ (Prompt-II), which have more complicated structure in case of ^{238}U and ^{232}Th , as α s of higher energies from these chains, compared to the ~ 5.3 MeV ^{210}Po α , can excite higher energy levels of ^{16}O . The smallest peak seen around ~ 5 MeV is due to the γ from $^{12}\text{C}^*$ de-excitation (Prompt-III). We remind that additional energy depositions from proton recoil or α before its capture can modify the reconstructed prompt energy. This energy scale is also not corrected for the intrinsic non-linearity effects in LS and is anchored at a 2.2 MeV γ energy-scale equivalent. The right column of figure 13 shows 2D distributions between the correlated reconstructed prompt-delayed time dT and distance dL . The mean dT of 0.215 ms is the same for ^{238}U and ^{232}Th chains and ^{210}Po . The mean dL for ^{210}Po of 0.689 m is smaller than the mean dL of 0.746 m for ^{238}U and 0.750 m for ^{232}Th due to different energies of $^{16}\text{O}^*$ de-excitation products with different ranges in LS.

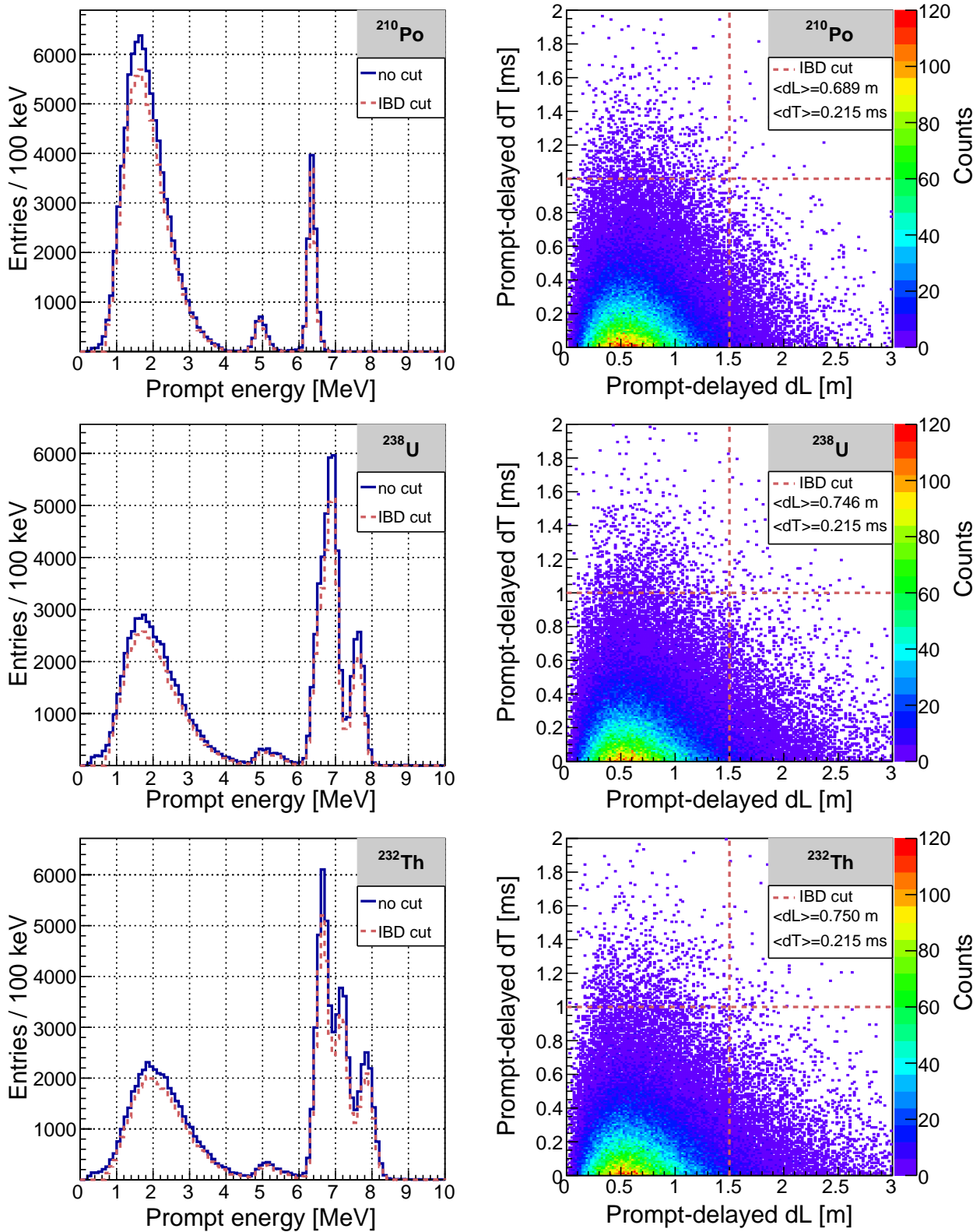


Fig. 13 Results of the $^{13}\text{C}(\alpha, n)^{16}\text{O}$ simulation with JUNO software for different α sources: ^{210}Po (top), ^{238}U chain (middle), and ^{232}Th chain (bottom). Left: The reconstructed prompt energy spectra before (solid blue line) and after (dashed red line) the IBD selection cuts. Right: The reconstructed prompt-delayed time dT and distance dL . The red dashed lines demonstrate the applied IBD selection cuts.

Table 3 Rates of IBD-like background events due to $^{13}\text{C}(\alpha, n)^{16}\text{O}$ reactions expected in JUNO from ^{238}U and ^{232}Th chains (minimal requirement for the NMO measurement) and from the expected ^{210}Po (from the ^{210}Pb contamination and stand-alone). Label “cpd” stands for counts per day and CD refers to the whole JUNO LS volume. The considered fiducial volume is a sphere of 17.2 m radius which corresponds to 18.35 kt of LS.

sources	Y_n [n/chain]	c [g/g]	R_α [cpd/kt]	$R_{(\alpha, n)}$ [cpd/CD]	$\mathcal{E}_{(\alpha, n)}^{\text{IBD}}$	$R_{(\alpha, n)}^{\text{IBD}}$ [cpd/FV]
^{238}U	6.36×10^{-7}	10^{-15}	1068	0.013	0.84	0.011
^{232}Th	8.58×10^{-7}	10^{-15}	352	0.006	0.84	0.005
$^{210}\text{Pb}/^{210}\text{Po}$	5.11×10^{-8}	5×10^{-23}	12265	0.012	0.87	0.011
^{210}Po	5.11×10^{-8}	3×10^{-22}	70400	0.071	0.87	0.063

7 $^{13}\text{C}(\alpha, n)^{16}\text{O}$ event rates

7.1 Estimated $^{13}\text{C}(\alpha, n)^{16}\text{O}$ event rates from individual α sources

The $^{13}\text{C}(\alpha, n)^{16}\text{O}$ event rates in the JUNO LS can be estimated in the following steps. For each individual source, we first evaluate the rate of α decays R_α in the LS, assuming secular equilibrium in the decay chains:

$$R_\alpha \left[\frac{\text{cpd}}{\text{kt}} \right] = c \left[\frac{\text{g}}{\text{g}} \right] \cdot \frac{N_A \left[\frac{1}{\text{mol}} \right]}{\tau [\text{day}] \cdot M \left[\frac{\text{g}}{\text{mol}} \right]} \cdot 10^9 \left[\frac{\text{g}}{\text{kt}} \right]. \quad (4)$$

The rate R_α is expressed in cpd per 1 kt. The expected concentration levels c of ^{238}U , ^{232}Th , and $^{210}\text{Pb}/^{210}\text{Po}$ are discussed in Sec. 3 and are expressed as the mass of mother isotope per gram of LS. The respective molar mass is M and lifetime τ , while N_A is Avogadro’s constant.

In the second step, the expected rates $R_{(\alpha, n)}$ of $^{13}\text{C}(\alpha, n)^{16}\text{O}$ background events in the whole JUNO detector can be expressed as:

$$R_{(\alpha, n)} \left[\frac{\text{cpd}}{\text{CD}} \right] = R_\alpha \left[\frac{\text{cpd}}{\text{kt}} \right] \cdot Y_n \left[\frac{n}{\text{chain}} \right] \cdot M_{\text{LS}} [\text{kt}], \quad (5)$$

where Y_n [n/chain] are the neutron yields per chain from table 2 and M_{LS} is the 20 kt mass of the JUNO LS. Finally, taking into account the efficiencies $\mathcal{E}_{(\alpha, n)}^{\text{IBD}}$, *i.e.*, the probability that the (α, n) reaction passes the IBD selection criteria, we express the final background rates $R_{(\alpha, n)}^{\text{IBD}}$ in the antineutrino measurement in the spherical FV of 17.2 m radius (18.35 kt) due to $^{13}\text{C}(\alpha, n)^{16}\text{O}$ reactions in JUNO. Rates of 0.011 cpd/FV and 0.005 cpd/FV are expected from the ^{238}U and ^{232}Th chains in secular equilibrium, respectively. The dominant contribution of 0.063 cpd/FV is evaluated from unsupported ^{210}Po and an additional 0.011 cpd/FV from the ^{210}Po from ^{210}Pb that is out of equilibrium with the ^{238}U chain. All the ingredients for this calculation are summarized in table 3. The overall $^{13}\text{C}(\alpha, n)^{16}\text{O}$ background expected in JUNO amounts to 0.090 cpd/FV and its shape is shown in figure 14.

7.2 Event rate uncertainties

In this section, we evaluate the sources of uncertainty due to detector response and characteristics. In Sec. 7.2.1 we discuss the precision with which the realistic contamination of the LS with α emitters can be determined. In Sec. 7.2.2 we evaluate the impact of the accuracy of the JUNO LS quenching effect. Section 7.2.3 summarizes all effects to provide an estimation of the total systematic uncertainty on our results, taking into account also the uncertainties presented in section 5.2 regarding the simulation of the $^{13}\text{C}(\alpha, n)^{16}\text{O}$ reaction with SaG4n.

7.2.1 Evaluating α source concentration

Table 3 summarises the expected measurable (α, n) event rates according to the assumed α source concentration levels within the LS. Therefore, the uncertainty in the predicted (α, n) rate depends directly on the uncertainty in the measured radioactivity concentration levels within the detector. A commonly used *in-situ* method to extract the concentration of the ^{238}U and ^{232}Th chains in secular equilibrium [42, 58], is through the rate measurement of their daughter decay pairs ^{214}Bi - ^{214}Po and ^{212}Bi - ^{212}Po , respectively. These Bi-Po event pairs consist of the β -decay of Bi, followed rapidly by the α -decay of Po, providing a possibility of coincident event tagging with high efficiency and purity. These samples also provide excellent data for tuning the α/β discrimination methods [59], that are also being implemented in JUNO [27].

The amount of out-of-equilibrium ^{210}Po can be identified directly via application of these α/β discrimination methods [11]. In this work, we assume that JUNO data will allow extracting the precision of the α emitters in the LS with an uncertainty of 5%.

7.2.2 Scintillation quenching factors

JUNOSW models the quenching effects in the LS energy response following the semi-empirical Birks’ law [60], with

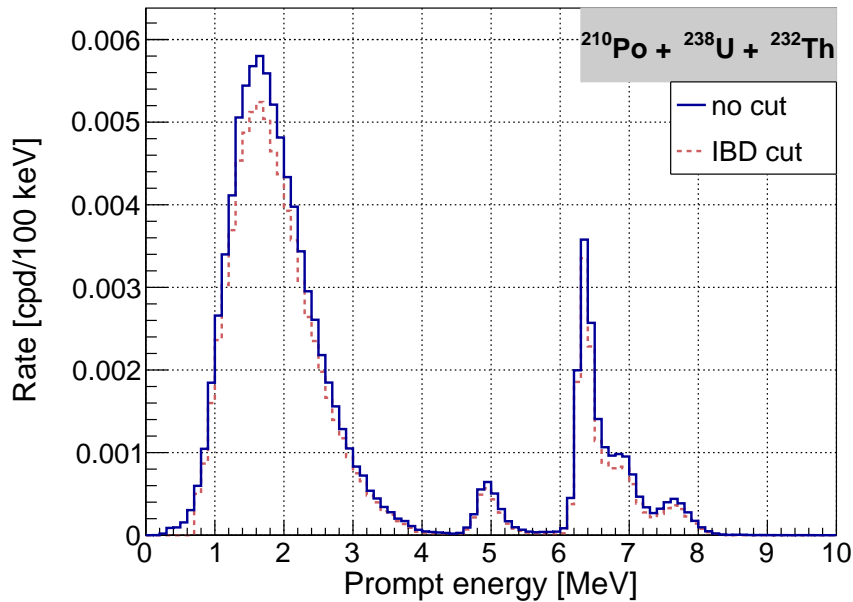


Fig. 14 The prompt reconstructed spectrum of the $^{13}\text{C}(\alpha, n)^{16}\text{O}$ reaction expected in JUNO before (solid blue line) and after (dashed red line) the IBD selection cuts, from the combined contributions of the ^{238}U , ^{232}Th , and ^{210}Po α sources, with assumed rates summarised in table 3.

three coefficients kB , defined for e^+/e^- , protons, and α s. The values of kB used in this work were assumed from measurements made by the Daya Bay experiment, where more details can be found in [24]. The thorough calibration of the quenching parameters in JUNO is planned based on deployable source calibration [34] and ongoing table-top experiments.

In this work, uncertainties in the proton quenching factors directly impact the low energy part of the prompt $^{13}\text{C}(\alpha, n)^{16}\text{O}$ spectrum. To determine the level at which the proton quenching uncertainty can impact the spectrum, we varied the Birks' coefficients within a range of $\pm 10\%$ in the simulation of ^{241}Am - ^{13}C neutron calibration source [61]. We performed multiple simulations of this source placed at the detector's center, accounting for its detailed geometry. For each simulation, the reconstructed prompt energy spectrum was produced, applying the same IBD analysis cuts defined in section 6.2. It was determined that the peak position of the low energy proton recoil peak can be defined with a precision of $\sim 1\%$.

The precision of the α quenching factor has limited impact on the (α, n) background. In order to evaluate it, we repeated our simulations by varying the kB values of α s by $\pm 5\%$, i.e. the precision certainly worse that JUNO expects to achieve on this parameter. The resulting changes in the (α, n) prompt reconstructed energy spectrum were found to be less than 1%.

Overall for this work, a 5% conservative uncertainty was assigned to the $^{13}\text{C}(\alpha, n)^{16}\text{O}$ event rates due to the quenching factors of protons and α s.

7.2.3 Summary of $^{13}\text{C}(\alpha, n)^{16}\text{O}$ event rate uncertainty

The sources of systematic uncertainties for the $^{13}\text{C}(\alpha, n)^{16}\text{O}$ event rates, following the above discussions, are summarised in table 4. The total value of 25% is calculated as the quadratic sum, conservatively neglecting possible correlations among different sources.

Table 4 Summary of the uncertainties of the estimated $^{13}\text{C}(\alpha, n)^{16}\text{O}$ event rates.

Uncertainty source	Relative uncertainty
SaG4n reference value discrepancy	18%
$^{13}\text{C}(\alpha, n)^{16}\text{O}$ cross section	15%
α maximum step length dependence	5%
Detector response	5%
Radioactivity concentration	5%
Total (quadratic sum)	25%

8 Conclusions

The $^{13}\text{C}(\alpha, n)^{16}\text{O}$ reaction represents an important background in the detection of electron antineutrinos in LS detectors, as for the cases of reactor and geoneutrinos. This work has presented the first specific evaluation of this interaction in JUNO, using novel techniques and implementing the expected radiopurity of its LS. In particular, we have

applied the SaG4n simulation tool version 1.3 and the current version of the JUNO simulation and reconstruction software. The total expected rate is $0.090 \times (1 \pm 0.25)$ cpd in the fiducial volume of the analysis (18.35 kt) from ^{232}Th and ^{238}U chains and additional out-of-equilibrium ^{210}Po , as in table 3. The expected shape of this background is shown in figure 14. While this evaluation has been performed specifically for JUNO using LAB-based LS, our results can be exploited also for other LS-based experiments. Particularly useful can be the provided neutron yields in table 3 and supplementary material available online regarding SaG4n simulation configurations and results for ^{232}Th , ^{238}U , and ^{210}Po , as well as the dependence of our results on the hydrogen mass fraction of the LS. And last but not least, this work employs one particular nuclear database, JENDL/AN-2005. Additional calculations using other newer libraries may be needed in the future. It will mainly help to more precisely evaluate the associated systematic uncertainties. Moreover, evaluation of the realistic background levels based on the JUNO data is also planned.

Acknowledgments

This work was supported by the Chinese Academy of Sciences, the National Key R&D Program of China, the Guangdong provincial government, the Tsung-Dao Lee Institute of Shanghai Jiao Tong University in China, the Institut National de Physique Nucléaire et de Physique de Particules (IN2P3) in France, the Istituto Nazionale di Fisica Nucleare (INFN) in Italy, the Fond de la Recherche Scientifique (F.R.S-FNRS) and the Institut Interuniversitaire des Sciences Nucléaires (IISN) in Belgium, the Conselho Nacional de Desenvolvimento Científico e Tecnológico in Brazil, the Agencia Nacional de Investigacion y Desarrollo and ANID - Millennium Science Initiative Program – ICN2019_044 in Chile, the European Structural and Investment Funds, the Czech Ministry of Education, Youth and Sports and the Charles University Research Center in Czech Republic, the Deutsche Forschungsgemeinschaft (DFG), the Helmholtz Association, and the Cluster of Excellence PRISMA+ in Germany, the Joint Institute of Nuclear Research (JINR) and Lomonosov Moscow State University in Russia, the Slovak Research and Development Agency in Slovak, MOST and MOE in Taipei, the Program Management Unit for Human Resources & Institutional Development, Research and Innovation, Chulalongkorn University, and Suranaree University of Technology in Thailand, the Science and Technology Facilities Council (STFC) in the UK, University of California at Irvine and the National Science Foundation in the US, and the State project “Science” by the Ministry of Science and Higher Education of the Russian Federation under the contract 075-15-2024-541.

References

1. C.L. Cowan, F. Reines, F.B. Harrison, H.W. Kruse, A.D. McGuire, *Science* **124**, 103 (1956). DOI 10.1126/science.124.3212.103
2. Y.J. Ko, et al., *Phys. Rev. Lett.* **118**(12), 121802 (2017). DOI 10.1103/PhysRevLett.118.121802
3. H. Almazán, et al., *Phys. Rev. D* **102**(5), 052002 (2020). DOI 10.1103/PhysRevD.102.052002
4. J. Ashenfelter, et al., *Nucl. Instrum. Meth. A* **922**, 287 (2019). DOI 10.1016/j.nima.2018.12.079
5. I. Alekseev, et al., *Phys. Lett. B* **787**, 56 (2018). DOI 10.1016/j.physletb.2018.10.038
6. F.P. An, et al., *Phys. Rev. Lett.* **130**(16), 161802 (2023). DOI 10.1103/PhysRevLett.130.161802
7. G. Bak, et al., *Phys. Rev. Lett.* **121**(20), 201801 (2018). DOI 10.1103/PhysRevLett.121.201801
8. H. de Kerret, et al., *Nature Phys.* **16**(5), 558 (2020). DOI 10.1038/s41567-020-0831-y
9. A. Gando, et al., *Phys. Rev. D* **88**(3), 033001 (2013). DOI 10.1103/PhysRevD.88.033001
10. S. Abe, et al., *Geophysical Research Letters* **49**(16), e2022GL099566 (2022). DOI 10.1029/2022GL099566
11. M. Agostini, et al., *Phys. Rev. D* **101**(1), 012009 (2020). DOI 10.1103/PhysRevD.101.012009
12. G. Bellini, et al., *Nature* **512**(7515), 383 (2014). DOI 10.1038/nature13702
13. V. Albanese, et al., *JINST* **16**(08), P08059 (2021). DOI 10.1088/1748-0221/16/08/P08059
14. A. Allegra, et al., *Eur. Phys. J. C* **85**(1), 17 (2025). DOI 10.1140/epjc/s10052-024-13687-5
15. F. An, et al., *J. Phys. G* **43**(3), 030401 (2016). DOI 10.1088/0954-3899/43/3/030401
16. A. Abusleme, et al., *Prog. Part. Nucl. Phys.* **123**, 103927 (2022). DOI 10.1016/j.pnpnp.2021.103927
17. A. Abusleme, et al., *Chin. Phys. C* **49**(3), 033104 (2025). DOI 10.1088/1674-1137/ad7f3e
18. K. Abe, et al., *Nucl. Instrum. Meth. A* **1027**, 166248 (2022). DOI 10.1016/j.nima.2021.166248
19. CIAAW. Isotopic abundances and atomic weight of carbon. Retrieved November 1, 2024 from <https://ciaaw.org/carbon.htm>
20. D. Cano-Ott, et al., White paper on (α, n) neutron yield calculations (2024). Preprint [arXiv:2405.07952v3](https://arxiv.org/abs/2405.07952v3)
21. F.P. An, et al., *Phys. Rev. D* **95**(7), 072006 (2017). DOI 10.1103/PhysRevD.95.072006
22. E. Mendoza, D. Cano-Ott, P. Romojaro, V. Alcayne, P. García Abia, V. Pesudo, L. Romero, R. Santorelli, *Nucl. Instrum. Meth. A* **960**, 163659 (2020). DOI 10.1016/j.nima.2020.163659
23. T. Lin, et al., *Eur. Phys. J. C* **83**(5), 382 (2023). DOI 10.1140/epjc/s10052-023-11514-x. [Erratum: *Eur.Phys.J.C* 83, 660 (2023)]

24. A. Abusleme, et al., *Chin. Phys. C* **49**(1), 013003 (2025). DOI 10.1088/1674-1137/ad83aa
25. National Nuclear Data Center, Brookhaven National Laboratory. Nudat 3.0 (nuclear structure and decay data). Retrieved August 1, 2024 from <https://www.nndc.bnl.gov/nudat3/>.
26. A. Abusleme, et al., *Nucl. Instrum. Meth. A* **988**, 164823 (2021). DOI 10.1016/j.nima.2020.164823
27. H. Rebber, L. Ludhova, B.S. Wonsak, Y. Xu, *JINST* **16**(01), P01016 (2021). DOI 10.1088/1748-0221/16/01/P01016
28. C. Landini, et al., *Nucl. Instrum. Meth. A* **1069**, 169887 (2024). DOI 10.1016/j.nima.2024.169887
29. A. Abusleme, et al., *Eur. Phys. J. C* **81**(11), 973 (2021). DOI 10.1140/epjc/s10052-021-09544-4
30. A. Abusleme, et al., *Nucl. Instrum. Meth. A* **1057**, 168680 (2023). DOI 10.1016/j.nima.2023.168680
31. J. Hui, et al., *JINST* **16**(08), T08008 (2021). DOI 10.1088/1748-0221/16/08/T08008
32. Y. Zhang, et al., *Nucl. Instrum. Meth. A* **988**, 164867 (2021). DOI 10.1016/j.nima.2020.164867
33. Y. Guo, et al., *JINST* **14**(09), T09005 (2019). DOI 10.1088/1748-0221/14/09/T09005
34. A. Abusleme, et al., *JHEP* **03**, 004 (2021). DOI 10.1007/JHEP03(2021)004
35. J. Zhao, et al., *Astrophys. J.* **965**(2), 122 (2024). DOI 10.3847/1538-4357/ad2bfd
36. A. Abusleme, et al., *JCAP* **10**, 022 (2023). DOI 10.1088/1475-7516/2023/10/022
37. A. Abusleme, et al., *JCAP* **01**, 057 (2024). DOI 10.1088/1475-7516/2024/01/057
38. A. Abusleme, et al., *JCAP* **10**, 033 (2022). DOI 10.1088/1475-7516/2022/10/033
39. A. Abusleme, et al., *Eur. Phys. J. C* **81**, 10 (2021). DOI 10.1140/epjc/s10052-021-09565-z
40. A. Abusleme, et al., *Eur. Phys. J. C* **85**(1), 5 (2025). DOI 10.1140/epjc/s10052-024-13638-0
41. D. Basilico, et al., *Phys. Rev. D* **108**(10), 102005 (2023). DOI 10.1103/PhysRevD.108.102005
42. G. Bellini, et al., *Phys. Rev. D* **89**(11), 112007 (2014). DOI 10.1103/PhysRevD.89.112007
43. M. Agostini, et al., *Phys. Rev. D* **100**(8), 082004 (2019). DOI 10.1103/PhysRevD.100.082004
44. S. Abe, et al., *Phys. Rev. Lett.* **100**, 221803 (2008). DOI 10.1103/PhysRevLett.100.221803
45. A. Abusleme, et al., *JHEP* **11**, 102 (2021). DOI 10.1007/JHEP11(2021)102
46. T. Murata, H. Matsunobu, K. Shibata, Evaluation of the (α, xn) reaction data for JENDL/AN-2005. Tech. Rep. JAEA-Research 2006-052, JAEA, Japan (2006). URL <https://doi.org/10.11484/jaea-research-2006-052>
47. S. Agostinelli, et al., *Nucl. Instrum. Meth. A* **506**, 250 (2003). DOI 10.1016/S0168-9002(03)01368-8
48. J. Allison, et al., *IEEE Trans. Nucl. Sci.* **53**, 270 (2006). DOI 10.1109/TNS.2006.869826
49. J. Allison, et al., *Nucl. Instrum. Meth. A* **835**, 186 (2016). DOI 10.1016/j.nima.2016.06.125
50. P. Mohr, *Phys. Rev. C* **97**(6), 064613 (2018). DOI 10.1103/PhysRevC.97.064613
51. S. Harissopulos, H.W. Becker, J.W. Hammer, A. Lagoyannis, C. Rolfs, F. Strieder, *Phys. Rev. C* **72**, 062801 (2005). DOI 10.1103/PhysRevC.72.062801
52. S. Westerdale, P.D. Meyers, *Nucl. Instrum. Meth. Phys. Res. A* **875**, 57 (2017). DOI 10.1016/j.nima.2017.09.007
53. M.B. Gromov, S. Westerdale, I.A. Goncharenko, A.S. Chepurinov, *Phys. At. Nucl.* **86**(2), 181 (2023). DOI 10.31857/S0044002723020083
54. A.C. Fernandes, A. Kling, G.N. Vlaskin, *EPJ Web Conf.* **153**, 07021 (2017). DOI 10.1051/epjconf/201715307021
55. Y. Wang, G. Cao, L. Wen, Y. Wang, *Eur. Phys. J. C* **82**(4), 329 (2022). DOI 10.1140/epjc/s10052-022-10288-y
56. A. Abusleme, et al., *Eur. Phys. J. C* **82**(12), 1168 (2022). DOI 10.1140/epjc/s10052-022-11002-8
57. A. Abusleme, et al., *Chin. Phys. C* **46**(12), 123001 (2022). DOI 10.1088/1674-1137/ac8bc9
58. A. Allega, et al., *Phys. Rev. D* **109**(7), 072002 (2024). DOI 10.1103/PhysRevD.109.072002
59. D. Basilico, et al., *Phys. Rev. D* **109**(11), 112014 (2024). DOI 10.1103/PhysRevD.109.112014
60. J.B. Birks, *Proceedings of the Physical Society. Section A* **64**(10), 874 (1951). DOI 10.1088/0370-1298/64/10/303
61. J. Liu, R. Carr, D.A. Dwyer, W.Q. Gu, G.S. Li, R.D. McKeown, X. Qian, R.H.M. Tsang, F.F. Wu, C. Zhang, *Nucl. Instrum. Meth. A* **797**, 260 (2015). DOI 10.1016/j.nima.2015.07.003